

NATIONAL UNIVERSITY OF HO CHI MINH CITY  
UNIVERSITY OF SCIENCE

UNDERGRADUATE THESIS

Hofstadter butterfly in transition metal  
dichalcogenide monolayers

Ho Chi Minh City, 2025

---

Student: Tran Khoi Nguyen  
Supervisor: Dr. Huynh Thanh Duc

# TABLE OF CONTENTS

<b>TABLE OF CONTENTS</b>	<b>1</b>
<b>LIST OF FIGURES</b>	<b>2</b>
<b>1 INTRODUCTION</b>	<b>3</b>
<b>2 METHOD</b>	<b>4</b>
2.1 Three-band tight binding method without magnetic field . . . . .	4
2.2 Three-band tight binding method under a magnetic field . . . . .	9
2.3 Spin-orbit coupling . . . . .	17
2.4 Landau levels . . . . .	17
2.5 Chern number and Quantum Hall effect . . . . .	21
2.5.1 Hall conductance . . . . .	21
2.5.2 Quantum Hall effect and Landau levels . . . . .	21
2.5.3 Solving the diophantine equation . . . . .	24
2.5.4 Wannier diagram . . . . .	25
<b>3 RESULT AND DISCUSSION</b>	<b>28</b>
<b>4 CONCLUSION AND FUTURE WORK</b>	<b>29</b>
<b>A matrix</b>	<b>30</b>
<b>B Harper's equation</b>	<b>31</b>
<b>C Cyclotron frequency for all band</b>	<b>34</b>
<b>REFERENCES</b>	<b>39</b>

## LIST OF FIGURES

2.1	Top view of monolayer $MX_2$ . The large sphere is $M$ atom and the small sphere is $X$ . . . . .	4
2.2	Band structure of monolayer $MoS_2$ along $\Gamma$ -K direction using (GGA) fitting parameters. . . . .	9
2.3	The TB model of TMDC with six neighbors atom $M$ . . . . .	11
2.4	Magnetic unit cell for TMD monolayers. . . . .	12
2.5	Hofstadter butterfly for one band $ dz\rangle \equiv  \phi_1^1(x, y)\rangle$ (left) and all band(right) with $q = 797$ and vary $p$ from 1 to $q$ with field strength $B_0 = 4.6928 \times 10^4$ T. Here on $x$ -axis represents the flux in units of quantum flux enclosed by the unit cell and $y$ -axis represents the Energy. . . . .	14
2.6	The Hofstadter's butterflies of $MX_2$ monolayers using GGA parameters from Table 1. . . . .	15
2.7	An easy and intuitive visualization of sub-matrix $h_0$ one band(a) and matrix $H$ all band(b) through standard plotter with $q = 20$ . (a): orange squares, dark blue squares and sky blue squares are equivalent to $\epsilon_1, 2t_0 \cos \zeta_1, t_0$ respectively. . . . .	16
2.8	Band structure of monolayer- $MoS_2$ along $\Gamma$ -K direction, SOC causes huge spin splittings in band-structure at $K$ and $-K$ points. . . . .	18
2.9	(a) Same plot as Fig 2.3 but we consider a small area and (b) is the Landau fan diagram show for the first $n = 30$ levels near the bottom of the conduction band for a magnetic field up to $B = 500T$ . The purple line in Fig 2.9(b) is supposed to be Fermi level. The Fermi energy is fixed at $E = 1.046$ eV. . . . .	20
2.10	QHE . . . . .	22
2.11	Từ trái sang phải là các Hofstadter butterfly, lần lượt là $q = 99$ và $q = 797$ . . . . .	24
2.12	Wannier diagram . . . . .	27
C.1	kết quả cho C.13 . . . . .	37

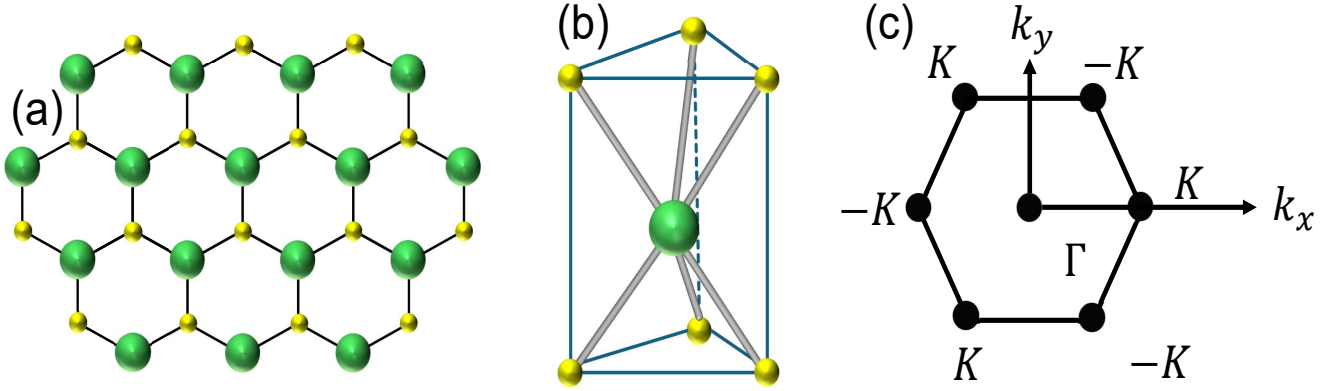
# CHƯƠNG 1

## INTRODUCTION

## CHƯƠNG 2

### METHOD

#### 2.1 Three-band tight binding method without magnetic field



Hình 2.1: Top view of monolayer  $MX_2$ . The large sphere is  $M$  atom and the small sphere is  $X$ .

The time-independent Schrödinger equation for an electron in the crystal has the form

$$\left[ -\frac{\hbar^2 \nabla^2}{2m} + U_0(\mathbf{r}) \right] \psi_{\lambda, \mathbf{k}}(\mathbf{r}) = \varepsilon_{\lambda}(\mathbf{k}) \psi_{\lambda, \mathbf{k}}(\mathbf{r}), \quad (2.1)$$

where  $U_0(\mathbf{r})$  is the periodic lattice potential,  $\psi_{\lambda, \mathbf{k}}(\mathbf{r})$  is the Bloch wavefunction of an electron in band  $\lambda$  with wave vector  $\mathbf{k}$  and  $\varepsilon_{\lambda}(\mathbf{k})$  is the band structure.

In the tight binding model (TBM), the single-electron Bloch wavefunction can be expressed in terms of atomic orbitals as follows

$$\psi_{\lambda, \mathbf{k}}(\mathbf{r}) = \sum_{j, i} C_{ji}^{\lambda}(\mathbf{k}) \sum_{\mathbf{R}} e^{i\mathbf{k} \cdot (\mathbf{R} + \mathbf{r}_i)} \phi_j(\mathbf{r} - \mathbf{R} - \mathbf{r}_i), \quad (2.2)$$

where  $\phi_j(\mathbf{r} - \mathbf{R} - \mathbf{r}_i)$  is the orbital  $j$  of an atom  $i$  localized on a lattice site  $\mathbf{R}$ , in which  $\mathbf{r}_i$  is the relative position of the atom  $i$  in the unit cell, and  $C_{ji}^\lambda(\mathbf{k})$  are the coefficients of linear expansion.

The unit cell of transition dichalcogenide(TMDC) monolayers involve one transition metal atom  $M$  and two chalcogenide atoms  $X$ . From the previous first principle calculations, it is shown that the electron states near the band edges of  $MX_2$  are mainly contributed from the three  $d$  orbital of  $M$  atom, namely  $d_{z^2}, d_{xy}, d_{x^2-y^2}$  [1]. This model is called the three-band tight binding model. The three orbitals's wave function of  $M$  atom are denoted as

$$|\phi_1\rangle = |d_{z^2}\rangle; \quad |\phi_2\rangle = |d_{xy}\rangle; \quad |\phi_3\rangle = |d_{x^2-y^2}\rangle. \quad (2.3)$$

The Bloch wavefunction in this model has the form

$$\psi_{\lambda,\mathbf{k}}(\mathbf{r}) = \sum_{j=1}^3 C_j^\lambda(\mathbf{k}) \sum_{\mathbf{R}} e^{i\mathbf{k}\cdot\mathbf{R}} \phi_j(\mathbf{r} - \mathbf{R}). \quad (2.4)$$

The coefficients  $C_j^\lambda(\mathbf{k})$  are the solutions of the eigenvalue equation

$$\sum_{jj'}^3 [H_{jj'}(\mathbf{k}) - \varepsilon_\lambda(\mathbf{k}) S_{jj'}(\mathbf{k})] C_j^\lambda(\mathbf{k}) = 0, \quad (2.5)$$

where

$$H_{jj'}(\mathbf{k}) = \sum_{\mathbf{R}} e^{i\mathbf{k}\cdot\mathbf{R}} \langle \phi_j(\mathbf{r}) | \left[ -\frac{\hbar^2 \nabla^2}{2m} + U_0(\mathbf{r}) \right] | \phi_{j'}(\mathbf{r} - \mathbf{R}) \rangle, \quad (2.6)$$

and

$$S_{jj'}(\mathbf{k}) = \sum_{\mathbf{R}} \langle \phi_j(\mathbf{r}) | \phi_{j'}(\mathbf{r} - \mathbf{R}) \rangle \approx \delta_{jj'}. \quad (2.7)$$

Three-band tight binding model takes into account the nearest neighbor hopping is called the three-band nearest-neighbor(NN) model. This model agrees well with the ab initio calculation for the band structure near the band edges, but the significantly deviate from the latter in other regions. This is because the three-band approximation neglects the  $p$  orbitals of  $X$  atoms which still have substantial contributions to the conduction bands at  $\Gamma$  and valence bands at  $M$ . The matrix elements of the TB Hamiltonian(pt)

are

$$H_{jj'}^{\text{NN}}(\mathbf{k}) = \mathcal{E}_{jj'}(\mathbf{0}) + e^{i\mathbf{k}\cdot\mathbf{R}_1}\mathcal{E}_{jj'}(\mathbf{R}_1) + e^{i\mathbf{k}\cdot\mathbf{R}_2}\mathcal{E}_{jj'}(\mathbf{R}_2) + e^{i\mathbf{k}\cdot\mathbf{R}_3}\mathcal{E}_{jj'}(\mathbf{R}_3) \\ + e^{i\mathbf{k}\cdot\mathbf{R}_4}\mathcal{E}_{jj'}(\mathbf{R}_4) + e^{i\mathbf{k}\cdot\mathbf{R}_5}\mathcal{E}_{jj'}(\mathbf{R}_5) + e^{i\mathbf{k}\cdot\mathbf{R}_6}\mathcal{E}_{jj'}(\mathbf{R}_6), \quad (2.8)$$

where

$$\mathcal{E}_{jj'}(\mathbf{R}) = \langle \phi_j(\mathbf{R}) | \left[ -\frac{\hbar^2 \nabla^2}{2m} + U_0 \mathbf{r} \right] | \phi_{j'}(\mathbf{r} - \mathbf{R}) \rangle, \quad (2.9)$$

and

$$\mathbf{R}_1 = (a, 0), \quad \mathbf{R}_2 = \left( \frac{a}{2}, -\frac{a\sqrt{3}}{2} \right), \quad \mathbf{R}_3 = \left( -\frac{a}{2}, -\frac{a\sqrt{3}}{2} \right), \\ \mathbf{R}_4 = (-a, 0), \quad \mathbf{R}_5 = \left( -\frac{a}{2}, \frac{a\sqrt{3}}{2} \right), \quad \mathbf{R}_6 = \left( \frac{a}{2}, \frac{a\sqrt{3}}{2} \right). \quad (2.10)$$

Here,  $\mathbf{R}_{1-6}$  are the positions of the nearest neighbors  $M$  atoms, see Fig.

$g_n$	$x'$	$y'$	$z'$	$z'^2$	$x'y'$	$\frac{1}{2}(x'^2 - y'^2)$
$E$	$x$	$y$	$z$	$z^2$	$xy$	$\frac{1}{2}(x^2 - y^2)$
$C_3(\frac{-2\pi}{3})$	$-\frac{1}{2}x + \frac{\sqrt{3}}{2}y$	$-\frac{\sqrt{3}}{2}x - \frac{1}{2}y$	$z$	$z^2$	$-\frac{1}{2}xy + \frac{\sqrt{3}}{4}(x^2 + y^2)$	$-\frac{\sqrt{3}}{2}xy - \frac{1}{4}(x^2 - y^2)$
$C_3(\frac{-4\pi}{3})$	$-\frac{1}{2}x - \frac{\sqrt{3}}{2}y$	$\frac{\sqrt{3}}{2}x + \frac{1}{2}y$	$z$	$z^2$	$-\frac{1}{2}xy - \frac{\sqrt{3}}{4}(x^2 + y^2)$	$\frac{\sqrt{3}}{2}xy - \frac{1}{4}(x^2 - y^2)$
$\sigma_\nu$	$-x$	$y$	$z$	$z^2$	$-xy$	$\frac{1}{2}(x^2 - y^2)$
$\sigma'_\nu$	$\frac{1}{2}x - \frac{\sqrt{3}}{2}$	$-\frac{\sqrt{3}}{2}x - \frac{1}{2}y$	$z$	$z^2$	$\frac{1}{2}xy - \frac{\sqrt{3}}{4}(x^2 + y^2)$	$-\frac{\sqrt{3}}{2}xy - \frac{1}{4}(x^2 - y^2)$
$\sigma''_\nu$	$\frac{1}{2}x + \frac{\sqrt{3}}{2}$	$\frac{\sqrt{3}}{2}x - \frac{1}{2}y$	$z$	$z^2$	$\frac{1}{2}xy + \frac{\sqrt{3}}{4}(x^2 + y^2)$	$\frac{\sqrt{3}}{2}xy - \frac{1}{4}(x^2 - y^2)$

Bảng 2.1: Some symmetry operators of the  $D_{3h}$  point group on basis functions taking  $(x, y, z)$  into  $(x', y', z')$ .  $C_3(\frac{-2\pi}{3})$  and  $C_3(\frac{-4\pi}{3})$  are the rotations by  $\frac{-2\pi}{3}$  and  $\frac{-4\pi}{3}$  around the  $z$  axis, respectively.  $\sigma_\nu$  is the reflection angular bisector of  $R_1$  and  $R_6$  in Fig. , and  $\sigma'_\nu, \sigma''_\nu$  are obtained through rotating  $\sigma_\nu$  around the  $z$  axis by  $2\pi/3$  and  $4\pi/3$ , respectively.

One parameterizes the matrices  $\mathcal{E}(\mathbf{0})$  and  $\mathcal{E}(\mathbf{R}_1)$  by

$$\mathcal{E}(\mathbf{0}) = \begin{pmatrix} \epsilon_1 & 0 & 0 \\ 0 & \epsilon_1 & 0 \\ 0 & 0 & \epsilon_2 \end{pmatrix}, \quad (2.11)$$

$$\mathcal{E}(\mathbf{R}_1) = \begin{pmatrix} t_0 & t_1 & t_2 \\ -t_1 & t_{11} & t_{12} \\ t_2 & -t_{12} & t_{22} \end{pmatrix}.$$

Given  $\mathcal{E}(\mathbf{R}_1)$ , the matrix  $\mathcal{E}(\mathbf{R}_{2-6})$  corresponding to all neighbor sites  $\mathbf{R}_{2-6}$  can be generated by

$$\mathcal{E}(g_n \mathbf{R}_1) = D(g_n) \mathcal{E}(\mathbf{R}_1) D^\dagger(g_n), \quad (2.12)$$

where  $D(g_n)$  is the matrix of the irreducible representation,  $g_n$  are symmetry operators of  $D_{3h}$  point groups,  $\{E, 2C_3, 3C_2, 2S_3, \sigma_h, 3\sigma_\nu\}$ . Particularly, we have  $\mathcal{E}(\mathbf{R}_2) = \mathcal{E}(\sigma'_\nu \mathbf{R}_1)$ ,  $\mathcal{E}(\mathbf{R}_3) = \mathcal{E}(C_3(-\frac{2\pi}{3}) \mathbf{R}_1)$ ,  $\mathcal{E}(\mathbf{R}_4) = \mathcal{E}(\sigma_\nu \mathbf{R}_1)$ ,  $\mathcal{E}(\mathbf{R}_5) = \mathcal{E}(C_3(-\frac{4\pi}{3}) \mathbf{R}_1)$ ,  $\mathcal{E}(\mathbf{R}_6) = \mathcal{E}(\sigma''_\nu \mathbf{R}_1)$ . Table 2.1 depicts the transformation of the basis functions under the action of symmetry operators. Also, from Table 2.1, we obtain irreducible matrices as follows

$$\begin{aligned} D(C_3(-\frac{2\pi}{3})) &= \begin{pmatrix} 1 & 0 & 0 \\ 0 & -1/2 & \sqrt{3}/2 \\ 0 & -\sqrt{3}/2 & -1/2 \end{pmatrix}, \quad D(C_3(-\frac{4\pi}{3})) = \begin{pmatrix} 1 & 0 & 0 \\ 0 & -1/2 & -\sqrt{3}/2 \\ 0 & \sqrt{3}/2 & -1/2 \end{pmatrix}, \\ D(\sigma_\nu) &= \begin{pmatrix} 1 & 0 & 0 \\ 0 & -1 & 0 \\ 0 & 0 & 0 \end{pmatrix}, \quad D(\sigma'_\nu) = \begin{pmatrix} 1 & 0 & 0 \\ 1 & 1/2 & -\sqrt{3}/2 \\ 0 & -\sqrt{3}/2 & -1/2 \end{pmatrix}, \\ D(\sigma''_\nu) &= \begin{pmatrix} 1 & 0 & 0 \\ 0 & 1/2 & \sqrt{3}/2 \\ 0 & \sqrt{3}/2 & -1/2 \end{pmatrix}. \end{aligned} \quad (2.13)$$

Therefore, we have

$$\begin{aligned} \mathcal{E}(\mathbf{R}_2) &= D(\sigma'_\nu) \mathcal{E}(\mathbf{R}_1) D^\dagger(\sigma'_\nu) \\ &= \begin{pmatrix} t_0 & \frac{1}{2}t_1 - \frac{\sqrt{3}}{2}t_2 & -\frac{\sqrt{3}}{2}t_1 - \frac{1}{2}t_2 \\ -\frac{1}{2}t_1 - \frac{\sqrt{3}}{2}t_2 & \frac{1}{4}t_{11} + \frac{3}{4}t_{22} & -\frac{\sqrt{3}}{4}t_{11} - t_{12} + \frac{\sqrt{3}}{4}t_{22} \\ \frac{\sqrt{3}}{2}t_1 - \frac{1}{2}t_2 & -\frac{\sqrt{3}}{4}t_{11} + t_{12} + \frac{\sqrt{3}}{4}t_{22} & \frac{3}{4}t_{11} + \frac{1}{4}t_{22} \end{pmatrix}, \end{aligned} \quad (2.14)$$

$$\begin{aligned} \mathcal{E}(\mathbf{R}_3) &= D(C(-\frac{2\pi}{3})) \mathcal{E}(\mathbf{R}_1) D^\dagger(C(-\frac{2\pi}{3})) \\ &= \begin{pmatrix} t_0 & -\frac{1}{2}t_1 + \frac{\sqrt{3}}{2}t_2 & -\frac{\sqrt{3}}{2}t_1 - \frac{1}{2}t_2 \\ \frac{1}{2}t_1 + \frac{\sqrt{3}}{2}t_2 & \frac{1}{4}t_{11} + \frac{3}{4}t_{22} & \frac{\sqrt{3}}{4}t_{11} + t_{12} - \frac{\sqrt{3}}{4}t_{22} \\ \frac{\sqrt{3}}{2}t_1 - \frac{1}{2}t_2 & \frac{\sqrt{3}}{4}t_{11} - t_{12} - \frac{\sqrt{3}}{4}t_{22} & \frac{3}{4}t_{11} + \frac{1}{4}t_{22} \end{pmatrix}, \end{aligned} \quad (2.15)$$

$$\mathcal{E}(\mathbf{R}_4) = D(\sigma_\nu) \mathcal{E}(\mathbf{R}_1) D^\dagger(\sigma_\nu) = \begin{pmatrix} t_0 & -t_1 & t_2 \\ t_1 & t_{11} & -t_{12} \\ t_2 & t_{12} & t_{22} \end{pmatrix}, \quad (2.16)$$

$$\begin{aligned} \mathcal{E}(\mathbf{R}_5) &= D(C(-\frac{4\pi}{3})) \mathcal{E}(\mathbf{R}_1) D^\dagger(C(-\frac{4\pi}{3})) \\ &= \begin{pmatrix} t_0 & -\frac{1}{2}t_1 - \frac{\sqrt{3}}{2}t_2 & \frac{\sqrt{3}}{2}t_1 - \frac{1}{2}t_2 \\ \frac{1}{2}t_1 - \frac{\sqrt{3}}{2}t_2 & \frac{1}{4}t_{11} + \frac{3}{4}t_{22} & -\frac{\sqrt{3}}{4}t_{11} + t_{12} + \frac{\sqrt{3}}{4}t_{22} \\ -\frac{\sqrt{3}}{2}t_1 - \frac{1}{2}t_2 & -\frac{\sqrt{3}}{4}t_{11} - t_{12} + \frac{\sqrt{3}}{4}t_{22} & \frac{3}{4}t_{11} + \frac{1}{4}t_{22} \end{pmatrix}, \end{aligned} \quad (2.17)$$



$$\begin{aligned}\mathcal{E}(\mathbf{R}_6) &= D(\sigma''_\nu)\mathcal{E}(\mathbf{R}_1)D^\dagger(\sigma''_\nu) \\ &= \begin{pmatrix} t_0 & \frac{1}{2}t_1 + \frac{\sqrt{3}}{2}t_2 & \frac{\sqrt{3}}{2}t_1 - \frac{1}{2}t_2 \\ -\frac{1}{2}t_1 + \frac{\sqrt{3}}{2}t_2 & \frac{1}{4}t_{11} + \frac{3}{4}t_{22} & \frac{\sqrt{3}}{4}t_{11} - t_{12} - \frac{\sqrt{3}}{4}t_{22} \\ -\frac{\sqrt{3}}{2}t_1 - \frac{1}{2}t_2 & \frac{\sqrt{3}}{4}t_{11} - t_{12} - \frac{\sqrt{3}}{4}t_{22} & \frac{3}{4}t_{11} + \frac{1}{4}t_{22} \end{pmatrix},\end{aligned}\quad (2.18)$$

The nearest-neighbor tight-binding Hamiltonian now can be written as

$$H^{\text{NN}}(\mathbf{k}) = \begin{pmatrix} h_0 & h_1 & h_2 \\ h_1^* & h_{11} & h_{12} \\ h_2^* & h_{12}^* & h_{22} \end{pmatrix} \quad (2.19)$$

where

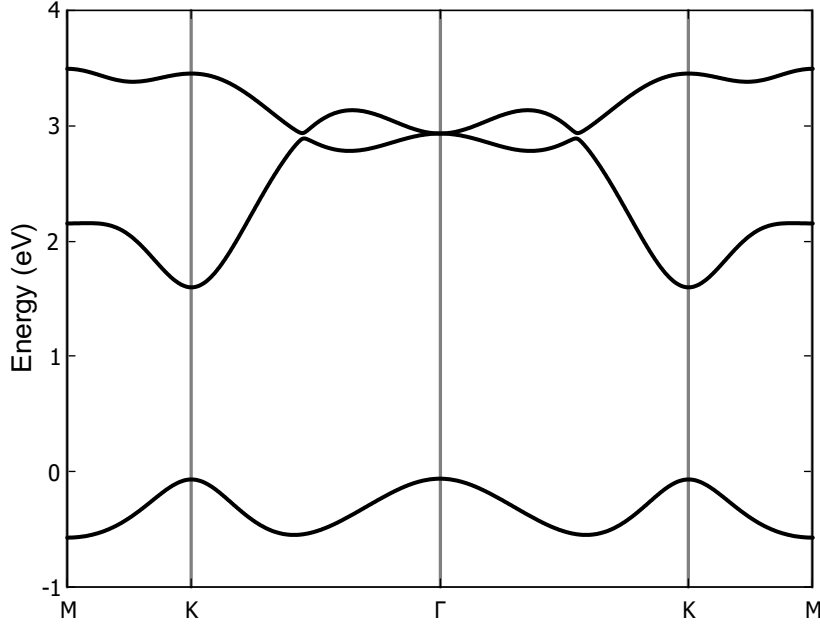
$$\begin{aligned}h_0 &= 2t_0 (\cos 2\alpha + 2 \cos \alpha \cos \beta) + \epsilon_1, \\ h_1 &= 2it_1 (\sin 2\alpha + \sin \alpha \cos \beta) - 2\sqrt{3}t_2 \sin \alpha \sin \beta, \\ h_2 &= 2t_2 (\cos 2\alpha - \cos \alpha \cos \beta) + 2i\sqrt{3}t_1 \cos \alpha \sin \beta, \\ h_{11} &= (t_{11} + 3t_{22}) \cos \alpha \cos \beta + 2t_{11} \cos 2\alpha + \epsilon_2, \\ h_{22} &= (3t_{11} + t_{22}) \cos \alpha \cos \beta + 2t_{22} \cos 2\alpha + \epsilon_2, \\ h_{12} &= \sqrt{3}(t_{22} - t_{11}) \sin \alpha \sin \beta + 4it_{12} \sin \alpha (\cos \alpha - \cos \beta),\end{aligned}\quad (2.20)$$

$$(\alpha, \beta) = \left( \frac{1}{2}k_x a, \frac{\sqrt{3}}{2}k_y a \right) \quad (2.21)$$

Eight additional parameters depicted in Table 2 are obtained by fitting the band with *ab initio* calculation results.

	$a(\text{\AA})$	$\epsilon_1$	$\epsilon_2$	$t_0$	$t_1$	$t_2$	$t_{11}$	$t_{12}$	$t_{22}$
MoS <sub>2</sub>	3.190	1.046	2.104	-0.184	0.401	0.507	0.218	0.338	0.057
WS <sub>2</sub>	3.191	1.130	2.275	-0.206	0.567	0.536	0.286	0.384	-0.061
MoSe <sub>2</sub>	3.326	0.919	2.065	-0.188	0.317	0.456	0.211	0.290	0.130
WSe <sub>2</sub>	3.325	0.943	2.179	-0.207	0.457	0.486	0.263	0.329	0.034
MoTe <sub>2</sub>	3.557	0.605	1.972	-0.169	0.228	0.390	0.207	0.239	0.252
WTe <sub>2</sub>	3.560	0.606	2.102	-0.175	0.342	0.410	0.233	0.270	0.190

Bảng 2.2: Fitted parameters in three-band nearest-neighbor tight-binding model for generalized-gradient approximation(GGA) cases for MX<sub>2</sub> [1].



Hình 2.2: Band structure of monolayer MoS<sub>2</sub> along  $\Gamma$ -K direction using (GGA) fitting parameters.

## 2.2 Three-band tight binding method under a magnetic field

Under a uniform magnetic field given by a vector potential  $\mathbf{A}(\mathbf{r})$  the single electron Hamiltonian changes into

$$H = \frac{(-i\hbar\nabla + e\mathbf{A}(\mathbf{r}))^2}{2m} + U_0(\mathbf{r}) + g^*\mu_B\mathbf{B} \cdot \mathbf{L}, \quad (2.22)$$

where  $\mu_B = \frac{e\hbar}{2m}$  is Bohr magneton,  $g^*$  is an effective Landé g-factor,  $\mathbf{B} = \nabla \times \mathbf{A}$  is the uniform magnetic field, and  $\mathbf{L}$  is the angular momentum. It is possible to add a phase factor to the tight binding wavefunction

$$\psi_{\lambda,\mathbf{k}}(\mathbf{r}) = \sum_{j=1}^3 C_j^\lambda \sum_{\mathbf{R}} e^{i(\mathbf{k} \cdot \mathbf{R} + \theta_{\mathbf{R}}(\mathbf{r}))} \phi_j(\mathbf{r} - \mathbf{R}). \quad (2.23)$$

We now have

$$H_{jj'}^{\text{NN}}(\mathbf{k}) = H_{jj'}(\mathbf{k}) + H_{jj'}^Z(\mathbf{k}), \quad (2.24)$$

where

$$\begin{aligned}
H_{jj'}(\mathbf{k}) &= \sum_{\mathbf{R}} \langle \phi_j(\mathbf{r}) | e^{-i\theta_0(\mathbf{r})} \left[ \frac{(-i\hbar\nabla + e\mathbf{A}(\mathbf{r}))^2}{2m} + U_0(\mathbf{r}) \right] e^{i(\mathbf{k}\cdot\mathbf{R} + \theta_{\mathbf{R}}(\mathbf{r}))} | \phi_{j'}(\mathbf{r} - \mathbf{R}) \rangle \\
&= \sum_{\mathbf{R}} \langle \phi_j(\mathbf{r}) | e^{i(\mathbf{k}\cdot\mathbf{R} + \theta_{\mathbf{R}} - \theta_0)} \left[ \frac{(-i\hbar\nabla + e\mathbf{A} + \hbar\nabla\theta_{\mathbf{R}})^2}{2m} + U_0(\mathbf{r}) \right] | \phi_{j'}(\mathbf{r} - \mathbf{R}) \rangle,
\end{aligned} \tag{2.25}$$

and

$$H_{jj'}^Z(\mathbf{k}) = g^* \mu_B \mathbf{B} \cdot \sum_{\mathbf{R}} \langle \phi_j(\mathbf{r}) | e^{i(\mathbf{k}\cdot\mathbf{R} + \theta_{\mathbf{R}} - \theta_0)} \mathbf{L} | \phi_{j'}(\mathbf{r} - \mathbf{R}) \rangle. \tag{2.26}$$

By choosing  $\theta_{\mathbf{R}} = -\frac{e}{\hbar} \int_{\mathbf{R}}^{\mathbf{r}} \mathbf{A}(\mathbf{r}') \cdot d\mathbf{r}'$  as Peierls substitution, the Hamiltonian in Eq. (4) now reads

$$\begin{aligned}
H_{jj'}(\mathbf{k}) &= \sum_{\mathbf{R}} \langle \phi_j(\mathbf{r}) | e^{i\mathbf{k}\cdot\mathbf{R} - \frac{ie}{\hbar} \int_{\mathbf{R}}^{\mathbf{r}} \mathbf{A}(\mathbf{r}') \cdot d\mathbf{r}' + \frac{ie}{\hbar} \int_0^{\mathbf{r}} \mathbf{A}(\mathbf{r}') \cdot d\mathbf{r}'} \left[ -\frac{\hbar^2 \nabla^2}{2m} + U_0(\mathbf{r}) \right] | \phi_{j'}(\mathbf{r} - \mathbf{R}) \rangle \\
&= \sum_{\mathbf{R}} e^{i\mathbf{k}\cdot\mathbf{R} + \frac{ie}{\hbar} \int_0^{\mathbf{R}} \mathbf{A}(\mathbf{r}') \cdot d\mathbf{r}'} \langle \phi_j(\mathbf{r}) | e^{-\frac{ie}{\hbar} \Phi_{\mathbf{R},\mathbf{r},0}} \left[ -\frac{\hbar^2 \nabla^2}{2m} + U_0(\mathbf{r}) \right] | \phi_{j'}(\mathbf{r} - \mathbf{R}) \rangle,
\end{aligned}$$

where  $\Phi_{\mathbf{R},\mathbf{r},0} = \oint_{\mathbf{R},\mathbf{r},0} \mathbf{A}(\mathbf{r}') \cdot d\mathbf{r}'$  is the closed loop line integral of  $\mathbf{A}$  along the triangle points  $\mathbf{R}, \mathbf{r}, \mathbf{0}$ , and  $\int_0^{\mathbf{R}} \mathbf{A}(\mathbf{r}') \cdot d\mathbf{r}'$  is the path integral along the two points  $\mathbf{R}, \mathbf{0}$ . Besides that, we have used the fact that

$$\int_{\mathbf{R}}^{\mathbf{r}} \mathbf{A}(\mathbf{r}') \cdot d\mathbf{r}' + \int_{\mathbf{r}}^{\mathbf{0}} \mathbf{A}(\mathbf{r}') \cdot d\mathbf{r}' = \Phi_{\mathbf{R},\mathbf{r},0} - \int_0^{\mathbf{R}} \mathbf{A}(\mathbf{r}') \cdot d\mathbf{r}'. \tag{2.27}$$

We can show that the flux term  $\Phi_{\mathbf{R},\mathbf{r},0}$  is negligibly small [2] by two observations. When  $\mathbf{r}$  is far away from the lattice points  $\mathbf{R}$  and  $\mathbf{0}$ , the flux is large but since the atomic orbitals are highly localized at these two lattice points, the value of the hopping term is very small and the whole hopping term goes to zero. While  $\mathbf{r}$  is at or near any of these lattice points, the triangle formed is small, and assuming small magnetic field, the flux term  $\Phi_{\mathbf{R},\mathbf{r},0}$  goes to zero, which giving us the Hamiltonian as

$$H_{jj'}(\mathbf{k}) = \sum_{\mathbf{R}} e^{i\mathbf{k}\cdot\mathbf{R} + \frac{ie}{\hbar} \int_0^{\mathbf{R}} \mathbf{A}(\mathbf{r}') \cdot d\mathbf{r}'} \langle \phi_j(\mathbf{r}) | \left[ -\frac{\hbar^2 \nabla^2}{2m} + U_0(\mathbf{r}) \right] | \phi_{j'}(\mathbf{r} - \mathbf{R}) \rangle, \tag{2.28}$$

$$H_{jj'}^Z(\mathbf{k}) = g^* \mu_B \mathbf{B} \cdot \sum_{\mathbf{R}} e^{i\mathbf{k}\cdot\mathbf{R} + \frac{ie}{\hbar} \int_0^{\mathbf{R}} \mathbf{A}(\mathbf{r}') \cdot d\mathbf{r}'} \langle \phi_j(\mathbf{r}) | \mathbf{L} | \phi_{j'}(\mathbf{r} - \mathbf{R}) \rangle. \tag{2.29}$$

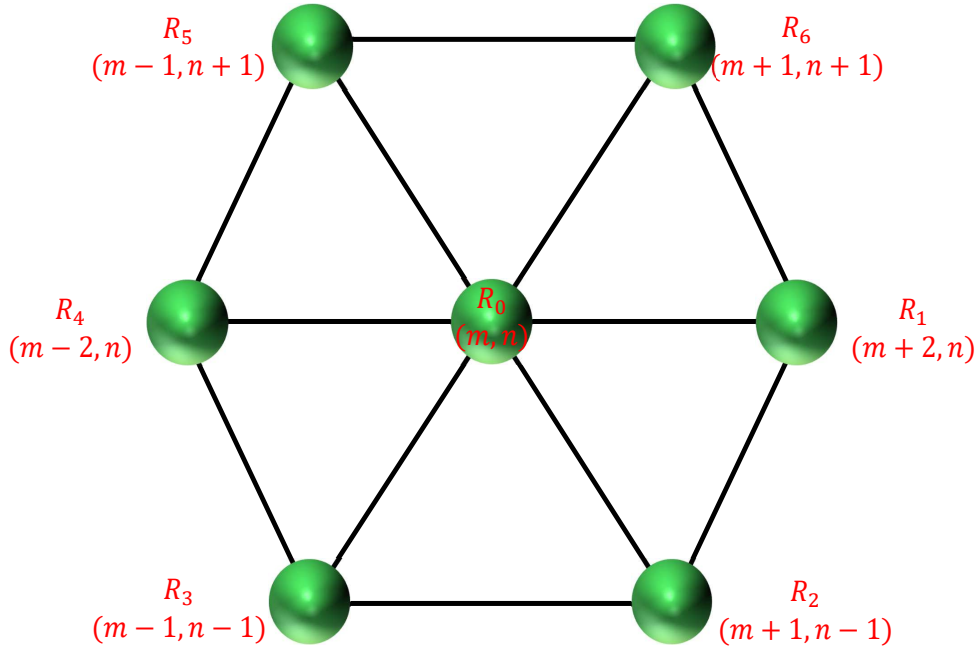
Considering only nearest neighbor(NN) hopping, Eq (2.9) becomes

$$\begin{aligned}
H_{jj'}(\mathbf{k}) &= \sum_{\mathbf{R}} e^{i(\mathbf{k} \cdot \mathbf{R} + \frac{e}{\hbar} \int_0^{\mathbf{R}} A(\mathbf{r}') d\mathbf{r}')} \mathcal{E}_{jj'}(\mathbf{R}) \\
&= \mathcal{E}_{jj'}(\mathbf{0}) + e^{i(\mathbf{k} \cdot \mathbf{R}_1 + \frac{e}{\hbar} \int_0^{\mathbf{R}_1} A(\mathbf{r}') d\mathbf{r}')} \mathcal{E}_{jj'}(\mathbf{R}_1) \\
&+ e^{i(\mathbf{k} \cdot \mathbf{R}_2 + \frac{e}{\hbar} \int_0^{\mathbf{R}_2} A(\mathbf{r}') d\mathbf{r}')} \mathcal{E}_{jj'}(\mathbf{R}_2) + e^{i(\mathbf{k} \cdot \mathbf{R}_3 + \frac{e}{\hbar} \int_0^{\mathbf{R}_3} A(\mathbf{r}') d\mathbf{r}')} \mathcal{E}_{jj'}(\mathbf{R}_3) \\
&+ e^{i(\mathbf{k} \cdot \mathbf{R}_4 + \frac{e}{\hbar} \int_0^{\mathbf{R}_4} A(\mathbf{r}') d\mathbf{r}')} \mathcal{E}_{jj'}(\mathbf{R}_4) + e^{i(\mathbf{k} \cdot \mathbf{R}_5 + \frac{e}{\hbar} \int_0^{\mathbf{R}_5} A(\mathbf{r}') d\mathbf{r}')} \mathcal{E}_{jj'}(\mathbf{R}_5) \\
&+ e^{i(\mathbf{k} \cdot \mathbf{R}_6 + \frac{e}{\hbar} \int_0^{\mathbf{R}_6} A(\mathbf{r}') d\mathbf{r}')} \mathcal{E}_{jj'}(\mathbf{R}_6).
\end{aligned} \tag{2.30}$$

In the presence of a perpendicular magnetic field  $\mathbf{B}\hat{z}$  to the plane of TMDC with the vector potential  $\mathbf{A} = (0, Bx, 0)$ . For convenience, let us switch to a shorthand notation for these extra terms and define

$$\begin{aligned}
\theta_{m,n}^{m',n'} &= \frac{e}{\hbar} \int_{m,n}^{m',n'} \mathbf{A} \cdot d\mathbf{r} \\
&= \frac{eB}{2\hbar} (x_{m'} + x_m)(y_{n'} - y_n).
\end{aligned} \tag{2.31}$$

In this system, hopping integral of  $x$ -direction does not change, but hopping integral of  $y$ -direction change and it depends on the  $x$  position. The crucial advantage of the Peierls phase approach is that lattice periodicity can be restored provided a suitable “magnetic supercell” containing several original unit cells is constructed.



Hình 2.3: The TB model of TMDC with six neighbors atom  $M$ .

With the given Landau gauge, the line integral  $\int \mathbf{A} \cdot d\mathbf{r}$  is evaluated to  $\int Bx dy$ .

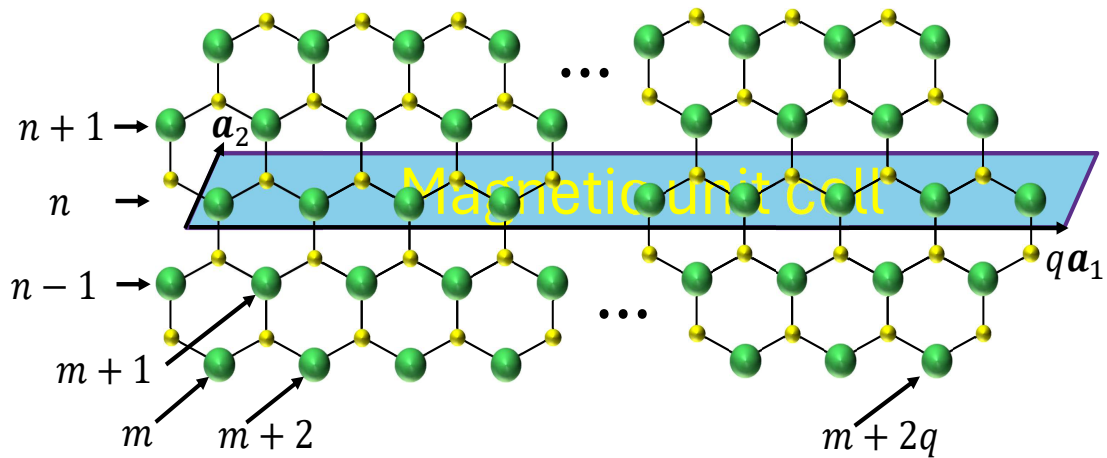
Let us now express the Hamiltonian from the zero-field are given by Eq. (2.31) with the transform hopping parameters, noting that the NN coordinates are  $x = \frac{ma}{2}(m = \pm 1, \pm 2)$  and  $y = \frac{na\sqrt{3}}{2}(n = 0, \pm 1)$ ,  $a$  being the lattice constant, are shown in Fig (2.2). Since  $dy = 0$  along the  $x$  direction,  $\theta_{m,n}^{m \pm 2, n} = 0$ , and using NN coordinates given for lattice site, the  $\theta_{m,n}^{m', n'}$  can be written as

$$\theta_{m,n}^{m', n'} = \begin{cases} 0 & m' = m \pm 2, n' = n, \\ \pm \frac{e}{\hbar} \frac{Ba^2\sqrt{3}}{4}(m + 1/2) & m' = m + 1, n' = n \pm 1, \\ \pm \frac{e}{\hbar} \frac{Ba^2\sqrt{3}}{4}(m - 1/2) & m' = m - 1, n' = n \pm 1. \end{cases} \quad (2.32)$$

The detail of this calculation can be checked in Appendix B. Identifying  $\frac{Ba^2\sqrt{3}}{4}$  as the magnetic flux  $\Phi$  passing through per unit cell and  $\hbar/e$  as the flux quantum  $\Phi_0$ , then we have

$$\begin{aligned} H_{jj'}(\mathbf{k}) = & E_{jj'}(\mathbf{0}) + e^{i\mathbf{k} \cdot \mathbf{R}_1} E_{jj'}(\mathbf{R}_1) + e^{-2i\pi(m+1/2)\Phi/\Phi_0} e^{i\mathbf{k} \cdot \mathbf{R}_2} E_{jj'}(\mathbf{R}_2) \\ & + e^{-2i\pi(m-1/2)\Phi/\Phi_0} e^{i\mathbf{k} \cdot \mathbf{R}_3} E_{jj'}(\mathbf{R}_3) + e^{i\mathbf{k} \cdot \mathbf{R}_4} E_{jj'}(\mathbf{R}_4) \\ & + e^{2i\pi(m-1/2)\Phi/\Phi_0} e^{i\mathbf{k} \cdot \mathbf{R}_5} E_{jj'}(\mathbf{R}_5) + e^{2i\pi(m+1/2)\Phi/\Phi_0} e^{i\mathbf{k} \cdot \mathbf{R}_6} E_{jj'}(\mathbf{R}_6). \end{aligned} \quad (2.33)$$

The Hamiltonian depends on the site index  $m$  and does not invariant under the translation of a lattice vector along the  $x$  axis. In order to restore this invariance, we can look at the case where the ratio of magnetic flux and flux quanta is a rational number  $\Phi/\Phi_0 = p/q$ . This mean, we can expand the unit cell in the  $x$  direction, the Hamiltonian becomes invariant under translational, allowing us to define what we will call the magnetic unit cell, which is consisting of  $q$   $M$ -atoms. This unit cell has lattice vectors  $q\mathbf{a}_1$  and  $\mathbf{a}_2$  as illustrated in Fig.



Hình 2.4: Magnetic unit cell for TMD monolayers.

We, now, define a new basis set of  $3q$  atomic orbitals  $\{\phi_j(\mathbf{r} - \mathbf{r}_i)\}$  where  $j = 1, 2, 3$

and  $i = 1, 2, \dots, q$ . Here,  $\mathbf{r}_i = (x_i, y_i) = m\mathbf{a}_1 + n\mathbf{a}_2$ . The Hamiltonian matrix in the new basis is written as

$$H_{ii'}^{jj'}(\mathbf{k}) = \sum_{\mathbf{R}} e^{i\mathbf{k} \cdot (\mathbf{R} + \mathbf{r}_{i'} - \mathbf{r}_i)} e^{\frac{ie}{\hbar} \int_0^{\mathbf{R}} \mathbf{A}(\mathbf{r}') \cdot d\mathbf{r}'} \langle \phi_j(\mathbf{r} - \mathbf{r}_i) | \left[ -\frac{\hbar^2 \nabla^2}{2m} + U_0 \right] | \phi_j(\mathbf{r} - \mathbf{R} - \mathbf{r}_{i'}) \rangle. \quad (2.34)$$

Taking the sum over  $\mathbf{R}$  and replacing  $\mathbf{r}_i = m\mathbf{a}_1 + n\mathbf{a}_2$ ,  $\mathbf{r}_{i'} = m'\mathbf{a}_1 + n'\mathbf{a}_2$ , and  $i = (m, n)$  with only considering the nearest-neighbors, we get

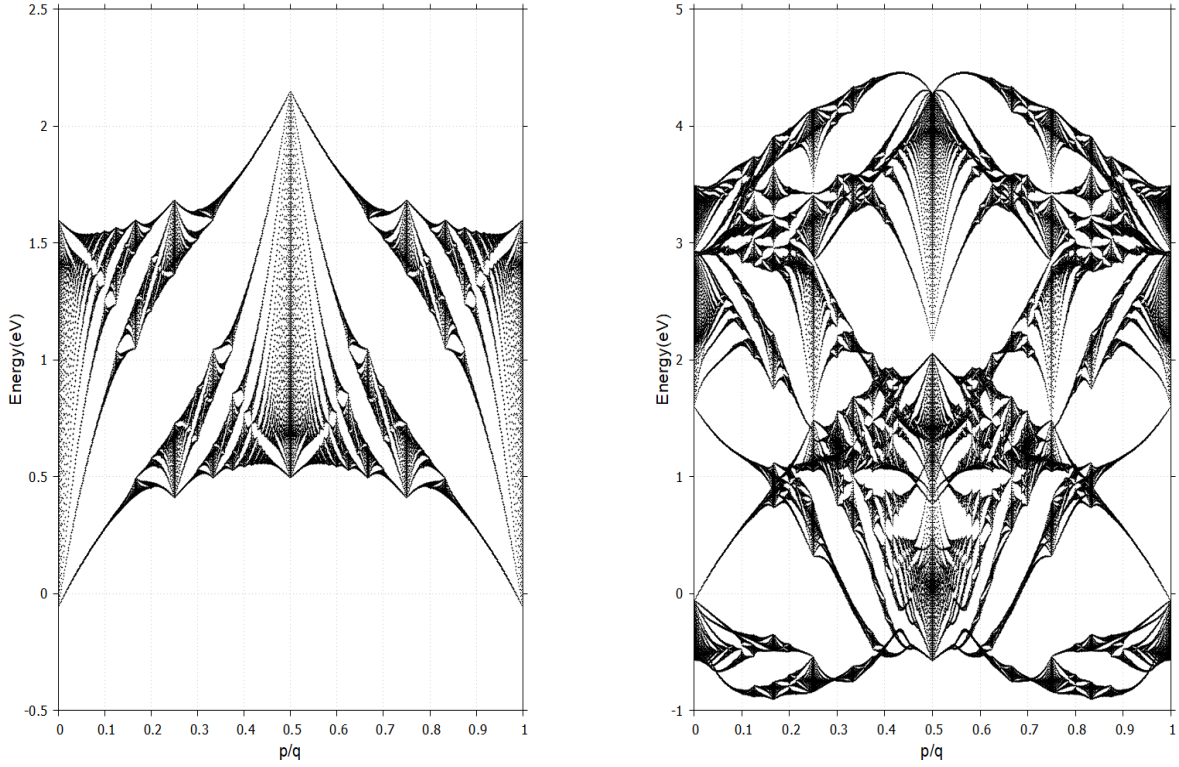
$$\begin{aligned} H_{ii'}^{jj'}(\mathbf{k}) = & \langle \phi_j(\mathbf{r} - m\mathbf{a}_1 - n\mathbf{a}_2) | \left[ -\frac{\hbar^2 \nabla^2}{2m} + U_0 \right] | \phi_j(\mathbf{r} - m\mathbf{a}_1 - n\mathbf{a}_2) \rangle \delta_{m,m'}^{n,n'} \\ & + e^{i\mathbf{k} \cdot \mathbf{a}_1} e^{i\theta_{m,n}^{m',n'}} \langle \phi_j(\mathbf{r} - m\mathbf{a}_1 - n\mathbf{a}_2) | \left[ -\frac{\hbar^2 \nabla^2}{2m} + U_0 \right] | \phi_j(\mathbf{r} - (m+2)\mathbf{a}_1 - n\mathbf{a}_2) \rangle \delta_{m+2,m'}^{n,n'} \\ & + e^{-i\mathbf{k} \cdot \mathbf{a}_1} e^{i\theta_{m,n}^{m',n'}} \langle \phi_j(\mathbf{r} - m\mathbf{a}_1 - n\mathbf{a}_2) | \left[ -\frac{\hbar^2 \nabla^2}{2m} + U_0 \right] | \phi_j(\mathbf{r} - (m-2)\mathbf{a}_1 - n'\mathbf{a}_2) \rangle \delta_{m-2,m'}^{n,n'} \\ & + e^{i\mathbf{k} \cdot \mathbf{a}_2} e^{i\theta_{m,n}^{m',n'}} \langle \phi_j(\mathbf{r} - m\mathbf{a}_1 - n\mathbf{a}_2) | \left[ -\frac{\hbar^2 \nabla^2}{2m} + U_0 \right] | \phi_j(\mathbf{r} - (m+1)\mathbf{a}_1 - (n+1)\mathbf{a}_2) \rangle \delta_{m',m+1}^{n',n+1} \\ & + e^{i\mathbf{k} \cdot (\mathbf{a}_2 - \mathbf{a}_1)} e^{i\theta_{m,n}^{m',n'}} \langle \phi_j(\mathbf{r} - m\mathbf{a}_1 - n\mathbf{a}_2) | \left[ -\frac{\hbar^2 \nabla^2}{2m} + U_0 \right] | \phi_j(\mathbf{r} - (m-1)\mathbf{a}_1 - (n+1)\mathbf{a}_2) \rangle \delta_{m',m-1}^{n',n+1} \\ & + e^{-i\mathbf{k} \cdot \mathbf{a}_2} e^{i\theta_{m,n}^{m',n'}} \langle \phi_j(\mathbf{r} - m\mathbf{a}_1 - n\mathbf{a}_2) | \left[ -\frac{\hbar^2 \nabla^2}{2m} + U_0 \right] | \phi_j(\mathbf{r} - (m-1)\mathbf{a}_1 - (n-1)\mathbf{a}_2) \rangle \delta_{m',m-1}^{n',n-1} \\ & + e^{i\mathbf{k} \cdot (-\mathbf{a}_2 + \mathbf{a}_1)} e^{i\theta_{m,n}^{m',n'}} \langle \phi_j(\mathbf{r} - m\mathbf{a}_1 - n\mathbf{a}_2) | \left[ -\frac{\hbar^2 \nabla^2}{2m} + U_0 \right] | \phi_j(\mathbf{r} - (m+1)\mathbf{a}_1 - (n-1)\mathbf{a}_2) \rangle \delta_{m',m+1}^{n',n-1}. \end{aligned} \quad (2.35)$$

Note that  $\mathbf{a}_1 = \mathbf{R}_1$ ,  $\mathbf{a}_2 = \mathbf{R}_6$ ,  $-\mathbf{a}_2 = \mathbf{R}_3$ ,  $\mathbf{a}_2 - \mathbf{a}_1 = \mathbf{R}_5$  and  $-\mathbf{a}_2 + \mathbf{a}_1 = \mathbf{R}_2$ . By substituting Eq (2.32) into Eq (2.35), consequently the Hamiltonian matrix in the new basis is written as

$$\begin{aligned} H_{ii'}^{jj'}(\mathbf{k}) = & E_{jj'}(\mathbf{0}) \delta_{m,m'}^{n,n'} + E_{jj'}(\mathbf{R}_1) \delta_{m+2,m'}^{n,n'} + e^{-2i\pi(m+1/2)p/q} E_{jj'}(\mathbf{R}_2) \delta_{m+1,m'}^{n-1,n'} \\ & + e^{-2i\pi(m-1/2)p/q} E_{jj'}(\mathbf{R}_3) \delta_{m-1,m'}^{n-1,n'} + E_{jj'}(\mathbf{R}_4) \delta_{m-2,m'}^{n,n'} \\ & + e^{2i\pi(m-1/2)p/q} e^{i\beta} E_{jj'}(\mathbf{R}_5) \delta_{m-1,m'}^{n+1,n'} + e^{2i\pi(m+1/2)p/q} e^{i\beta} E_{jj'}(\mathbf{R}_6) \delta_{m+1,m'}^{n+1,n'}. \end{aligned} \quad (2.36)$$

Now, for given flux ratio  $p/q$ , only the  $q$  determines the periodicity of the magnetic cell assuming  $p$  and  $q$  are mutually prime numbers. When we plot the band energies while varying the  $p$ , we obtain the famous Hofstadter butterfly [3], a complex fractal structure as seen in Fig. 2.3. This structure is generated at the  $K = (\frac{4\pi}{3a}, 0)$  k-point. This fractal spectrum is a result of two competing effects, lattice periodicity and magnetic unit cell

periodicity enforced by the presence of the magnetic field. Eq. 2.16 give the following matrix which must be diagonalized to obtain the energy eigenvalues.



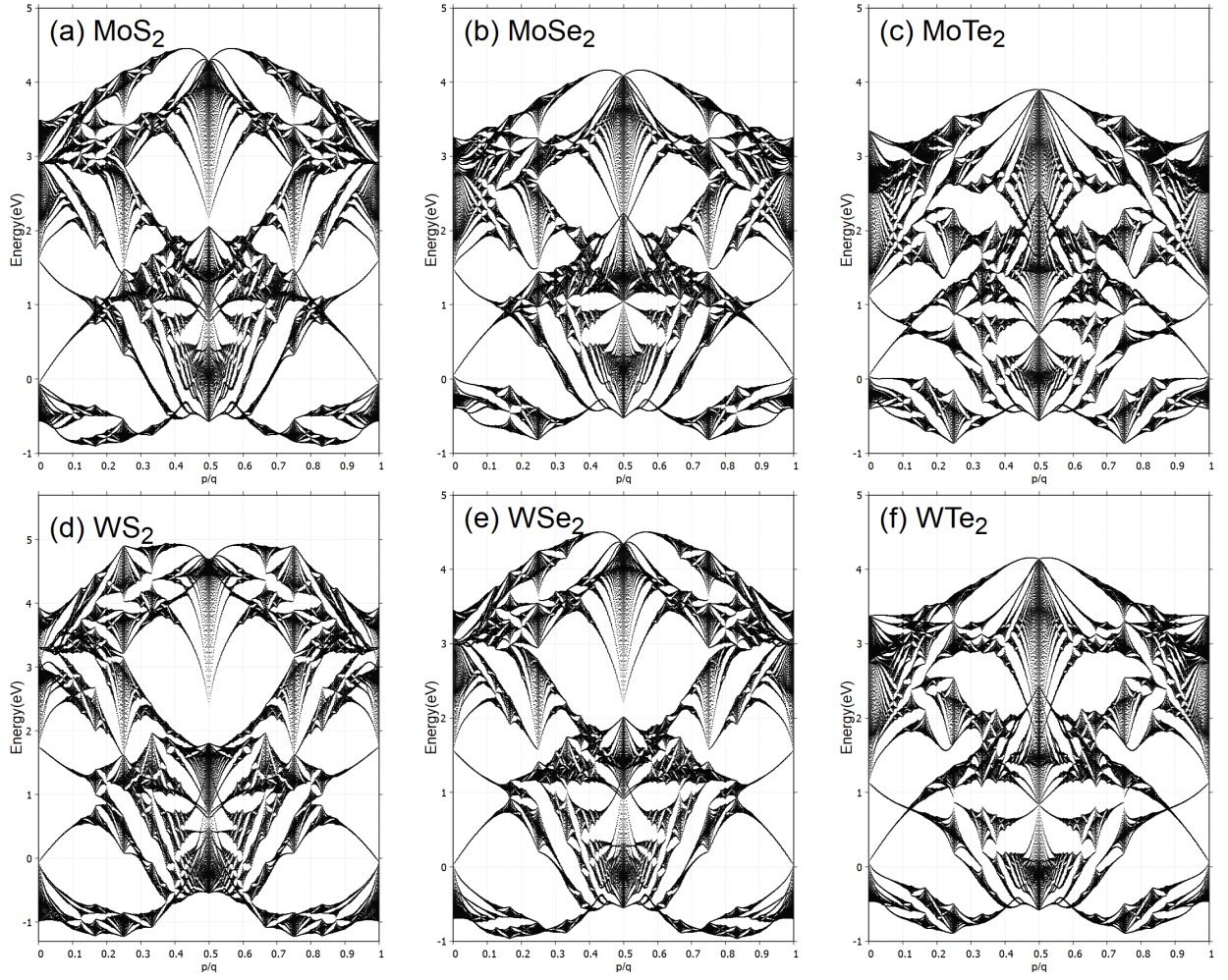
Hình 2.5: Hofstadter butterfly for one band  $|dz\rangle \equiv |\phi_1^1(x, y)\rangle$ (left) and all band(right) with  $q = 797$  and vary  $p$  from 1 to  $q$  with field strength  $B_0 = 4.6928 \times 10^4$  T. Here on  $x$ -axis represents the flux in units of quantum flux enclosed by the unit cell and  $y$ -axis represents the Energy.

The magnetic field enters the TB Hamiltonian only through the fraction  $p/q$ , which is the magnetic flux through the primitive unit cell of the lattice. In general, as the lattice geometry evolves, the area of the primitive unit cell changes  $(m + 1/2)$  times.

The spectrum has various symmetries: It is only show that the flux  $q$  is affects the spectrum, so if  $p/q$  changed to  $p/q + c$  while  $c$  any interger, the spectrum is unchanged. The spectrum is also unchanged on changing  $p/q$  to  $-p/q$ , because if  $\psi$  is an eigenstate withe energy for field  $p/q$ , then its complex conjugate  $\psi^*$  is an engenstate with the same energy for field  $-p/q$ . These two symmetries are not special to the  $MX_2$ 's case. The third symmetry is that if  $p/q$  is changed to  $p/q + 1/2$ , this is the same as changing  $t_i$ , which are hopping energies, to  $-t_i$ , this leads to the inverting of the spectrum.

Before we end the section, a few general remarks are in order. The role of the eight hopping constants  $t$  is just to set an energy scale. Change the hopping constants amounts to stretching the butterfly spectrum vertically, which is an overall scaling to the energy levels. Thus it does not give rise to any interesting physical phenomenon.





Hình 2.6: The Hofstadter's butterflies of  $MX_2$  monolayers using GGA parameters from Table 1.

Using Eq (2.16), we obtain the eigenvalue equation  $H\phi_\mu^j = E\phi_\mu^j$  and

$$H = \begin{pmatrix} h_0 & h_1 & h_2 \\ h_1^* & h_{11} & h_{12} \\ h_2^* & h_{12}^* & h_{22} \end{pmatrix} \quad (2.37)$$

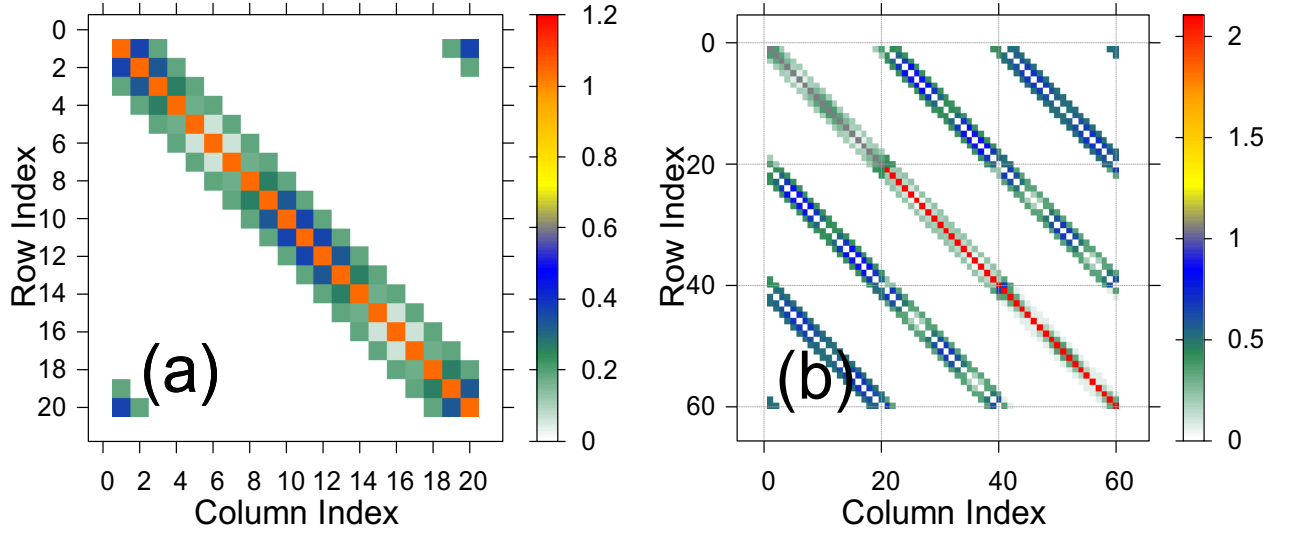
where

$$h_0 = \begin{pmatrix} \epsilon_1 & A_1 & t_0 & 0 & \cdots & 0 & t_0 & B_1 \\ B_2 & \epsilon_1 & A_2 & t_0 & 0 & \cdots & 0 & t_0 \\ t_0 & B_3 & \epsilon_1 & A_3 & t_0 & 0 & \cdots & 0 \\ \vdots & \vdots & \vdots & \ddots & \vdots & \vdots & \vdots & \vdots \\ t_0 & 0 & \cdots & 0 & t_0 & B_{q-1} & \epsilon_1 & A_{q-1} \\ A_q & t_0 & \cdots & 0 & 0 & t_0 & B_q & \epsilon_1 \end{pmatrix} \quad (2.38)$$



$$h_1 = \begin{pmatrix} 0 & 2t_1 \cos \zeta_1 & t_1 & 0 & \cdots & 0 & -t_1 & -2t_1 \cos \gamma_1 \\ & +i\sqrt{3}t_2 \sin \zeta_1 & & & & & & -i\sqrt{3}t_2 \sin \gamma_1 \\ -2t_1 \cos \gamma_2 & 0 & 2t_1 \cos \zeta_2 & t_1 & 0 & \cdots & 0 & -t_1 \\ -i\sqrt{3}t_2 \sin \gamma_2 & & +i\sqrt{3}t_2 \sin \zeta_2 & & & & & \\ -t_1 & -2t_1 \cos \gamma_3 & 0 & 2t_1 \cos \zeta_3 & t_1 & 0 & \cdots & 0 \\ \vdots & \vdots & \vdots & \vdots & \vdots & \vdots & \vdots & \vdots \\ t_1 & 0 & \cdots & 0 & -t_1 & -2t_1 \cos \gamma_{q-1} & 0 & 2t_1 \cos \zeta_{q-1} \\ & & & & & -i\sqrt{3}t_2 \sin \gamma_{q-1} & & +i\sqrt{3}t_2 \sin \zeta_{q-1} \\ 2t_1 \cos \zeta_q & t_1 & \cdots & 0 & 0 & -t_1 & -2t_1 \cos \gamma_q & 0 \\ +i\sqrt{3}t_2 \sin \zeta_q & & & & & & -i\sqrt{3}t_2 \sin \gamma_q & \end{pmatrix} \quad (2.39)$$

$A_m = 2t_0 \cos \zeta_1$  in which  $\cos \zeta_m = \cos [\beta + 2\pi(m + 1/2)p/q]$  and  $\sin \gamma_m = \sin [\beta + 2\pi(m - 1/2)p/q]$  and  $h_0, h_1, h_2, h_{11}, h_{12}, h_{22}$  are sub-matrices have size  $q \times q$ . (A visualization is shown in Fig (2.4))



Hình 2.7: An easy and intuitive visualization of sub-matrix  $h_0$  one band(a) and matrix  $H$  all band(b) through standard plotter with  $q = 20$ . (a): orange squares, dark blue squares and sky blue squares are equivalent to  $\epsilon_1, 2t_0 \cos \zeta_1, t_0$  respectively.

An alternative approach to the derivation of the Hamiltonian under an uniform magnetic field is given in Appendix B.

## 2.3 Spin-orbit coupling

Due to the heavy mass of the transition-metal  $M$  atom, its spin orbit coupling(SOC) can be large. For the sake of simplicity, only the on-site contribution, namely, the  $\mathbf{L} \cdot \mathbf{S}$  term from  $M$  atoms. Using the bases  $\left\{ |d_{z^2}, \uparrow\rangle, |d_{xy}, \uparrow\rangle, |d_{x^2-y^2}, \uparrow\rangle, |d_{z^2}, \downarrow\rangle, |d_{xy}, \downarrow\rangle, |d_{x^2-y^2}, \downarrow\rangle \right\}$ , we get the SOC contribution to the Hamiltonian as

$$H' = \lambda \mathbf{L} \cdot \mathbf{S} = \frac{\lambda}{2} \begin{pmatrix} L_z & L_x - iL_y \\ L_x + iL_y & -L_z \end{pmatrix}, \quad (2.40)$$

in which

$$L_z = \begin{pmatrix} 0 & 0 & 0 \\ 0 & 0 & 2i \\ 0 & -2i & 0 \end{pmatrix} \quad (2.41)$$

is the matrix of  $\hat{L}_z$  ( $z$  component of the orbital angular momentum) in bases of  $d_{z^2}, d_{xy}, d_{x^2-y^2}$  and  $\lambda$  is characterized the strength of the SOC. Noting that, under the three bases, the matrix elements of  $\hat{L}_x$  and  $\hat{L}_y$  are all zeros. There for the Hamiltonian for the magnetic unit cell with the SOC as follows

$$\begin{aligned} H_{\text{SOC}}(\mathbf{k}) &= \mathbf{I}_2 \otimes H_0(\mathbf{k}) + H' \\ &= \begin{pmatrix} H_{3q \times 3q}(\mathbf{k}) + \frac{\lambda}{2} L_z & 0 \\ 0 & H_{3q \times 3q}(\mathbf{k}) - \frac{\lambda}{2} L_z \end{pmatrix} \end{aligned} \quad (2.42)$$

## 2.4 Landau levels

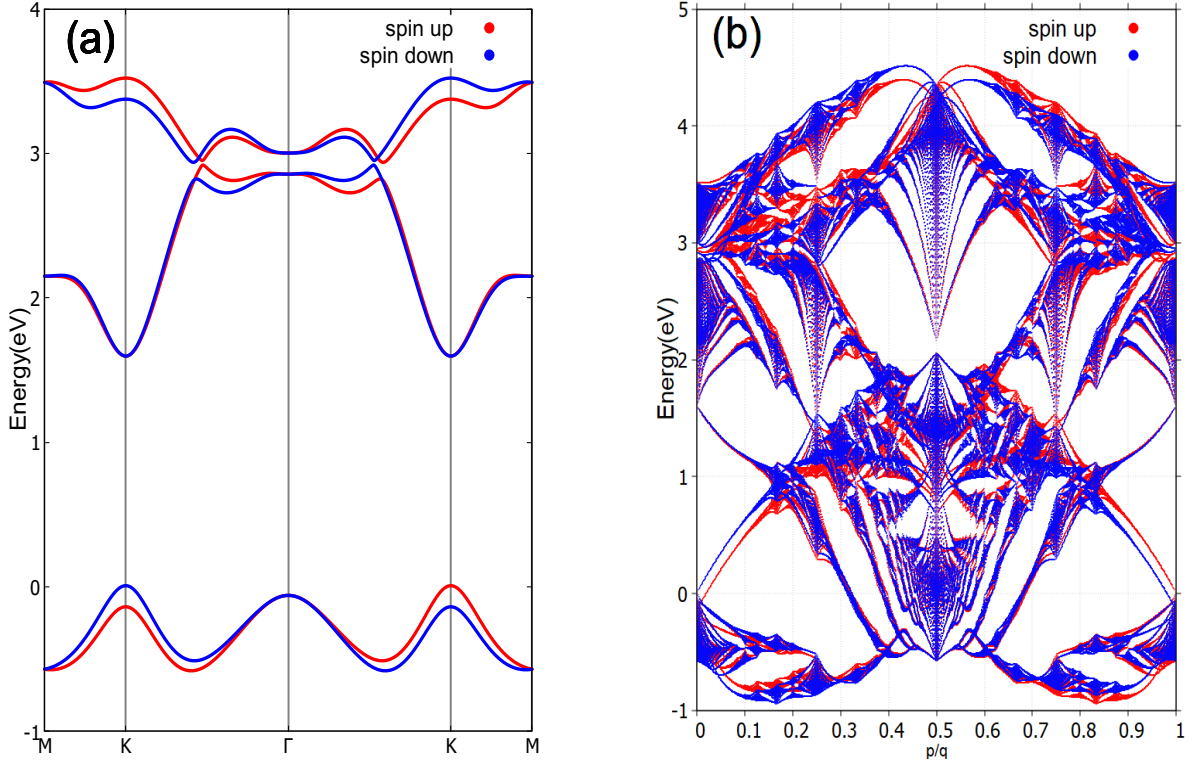
In solid-state physics, the behavior of electrons in magnetic fields is usually introduced by using the Hamiltonian

$$H = \frac{\mathbf{p} + e\mathbf{A}(\mathbf{r})^2}{2m}, \quad (2.43)$$

and the energy eigenfunctions are known as Landau levels

$$E_n = (n + 1/2) \hbar \omega_c. \quad (2.44)$$

This treatment is for free electrons, but near the bottom of the two-dimensional tight-binding band of TMD we must find a regime in which the electron behaves as a



Hình 2.8: Band structure of monolayer-MoS<sub>2</sub> along  $\Gamma$ -K direction, SOC causes huge spin splittings in band-structure at  $K$  and  $-K$  points.

nearly on. (At least with a nearly free dispersion relation).

Recalling the result obtained for the dispersion relation of an electron within the tight binding model

$$h_0 = 2t_0(\cos 2\alpha + 2 \cos \alpha \cos \beta) + \epsilon_1 \quad (2.45)$$

The dispersion energy is approximately free-electron-like by Taylor expansion to second order of  $\mathbf{k}$

$$\begin{aligned} H(\mathbf{k}) &\approx 2t_0 \left[ 1 - \frac{a^2 k_x^2}{2} + 2 \left( 1 - \frac{a^2 k_x^2}{8} \right) \left( 1 - \frac{3a^2 k_y^2}{8} \right) \right] \\ &= t_0 \frac{3}{16} (32 + a^4 k_x^2 k_y^2) - t_0 \frac{3}{2} a^2 (k_x^2 + k_y^2) + \epsilon_1, \end{aligned} \quad (2.46)$$

the first term  $a^2$  is negligibly small and another can be treated like constant, then we have

$$H(\mathbf{k}) \approx 6t_0 - \frac{3}{2} t_0 a^2 (k_x^2 + k_y^2) + \epsilon_1. \quad (2.47)$$

One of the ways derivation of effective mass  $m^*$  is substitution  $\mathbf{k} \rightarrow \mathbf{p} + e\mathbf{A}$ , with Landau

gauge  $\mathbf{A} = (0, Bx, 0)$

$$\begin{aligned} H(\mathbf{p}) &\approx 6t_0 - \frac{3}{2}t_0 \frac{a^2}{\hbar^2} \left[ p_x^2 + (p_y + eBx)^2 \right] + \epsilon_1 \\ &\approx 6t_0 - \frac{3}{2}t_0 \frac{a^2}{\hbar^2} p_x^2 - \frac{3}{2}t_0 \frac{a^2}{\hbar^2} (eB)^2 \left[ x - \left( -\frac{\hbar k_y}{eB} \right) \right]^2 + \epsilon_1. \end{aligned} \quad (2.48)$$

The Eq (2.24) can be rewrite in the form as

$$E(\mathbf{p}) = 6t_0 - \left[ \frac{1}{2m^*} p_x^2 + \frac{1}{2} m^* \omega_c^2 (x - x_0)^2 \right] + \epsilon_1, \quad (2.49)$$

where  $m^* = \frac{\hbar^2}{(3t_0 a^2)}$  is the effective mass and  $x_0 = \frac{\hbar k_y}{eB}$ . Hence, the cyclotron frequency is

$$\omega_c = \frac{eB}{m^*} = \frac{8\pi\sqrt{3}t_0 p}{\hbar q}, \quad (2.50)$$

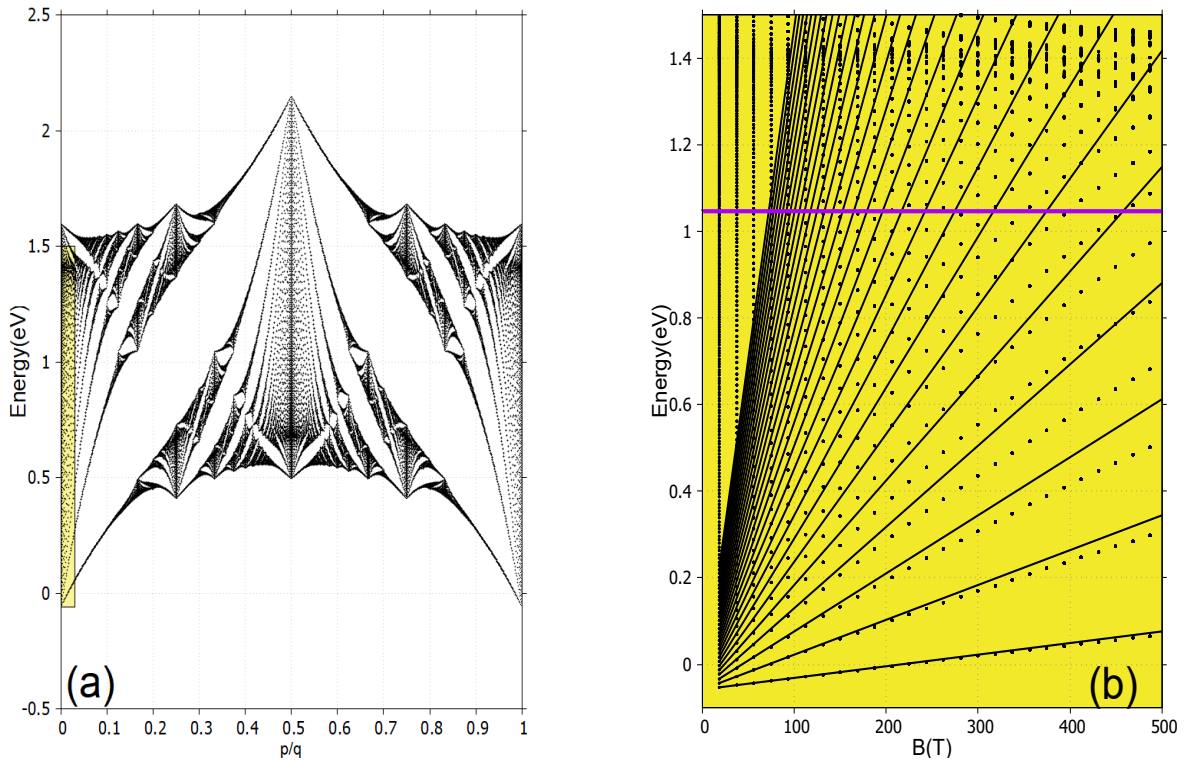
and therefore the Landau levels near the bottom of the band  $|d_{z^2}\rangle$  can be written as

$$\begin{aligned} E &= 6t_0 - \hbar\omega_c(n + 1/2) + \epsilon_1 \\ &= t_0 \left( 6 - 8\pi\sqrt{3}\frac{p}{q}(n + 1/2) \right) + \epsilon_1, \end{aligned} \quad (2.51)$$

in linear order of an uniform-flux, where  $n$  is Landau index. These levels give rise to what is called “The Landau fan”, being very important in the de Haas-van Alphen and Shubnikov-de Haas effects [4] which predicts oscillations of the magnetic moment of a metal depending on an applied magnetic field.

In Fig 2.7 we compare the spectrum of a small section of triangular lattice with  $p/q = 1/797$ , which is equivalent to small magnetic field, the spectrum of MoS<sub>2</sub>, with the energy of Landau levels given by Eq.(2.38) show standard equally spaced Landau levels [5–8] near the bottom of the bands, as plotted in Fig 2.7(b). The fan of Landau levels can be clearly seen emergin from the partern in Fig 2.4(a). In our model study, Landau levels can be classified into specific groups. In each group, each levels can be further labeled by a Landau index  $n$ .

In Fig 2.7, there is just one band in case zero field, with the effective mass  $m^* = \frac{\hbar}{3t_0 a^2}$ . The numerical result for this portion of the spectrum are shown in Fig 2.7 for  $p/q \geq 1/797$ . The first few Landau levels are clearly seen, and the asymptotic slopes  $p/q$  at large  $q$  given by Eq. (2.38) are shown for comparison for the first five Landau levels at  $B \leq 100$  T. At the values of  $B$  the fit is not ideal, but it does seem to be improving



Hình 2.9: (a) Same plot as Fig 2.3 but we consider a small area and (b) is the Landau fan diagram show for the first  $n = 30$  levels near the bottom of the conduction band for a magnetic field up to  $B = 500\text{T}$ . The purple line in Fig 2.9(b) is supposed to be Fermi level. The Fermi energy is fixed at  $E = 1.046\text{ eV}$ .

with the decreasing  $p/q$ .

Figure 2.4 displays a blowup of the low uniform magnetic region and the LLs as a function of  $\Phi/\Phi_0$  [9]. The Fermi energy is supposed to be for  $E_F = 1.046\text{ eV}$ , this is, is plotted for one-half spectrum. The Landau levels are all close to being linear in  $B$ , resulting from the magnetic quantization of parabolic bands at  $B = 0\text{ T}$  i.e. increasing values of  $B$ , these Landau levels are sequentially depleted; for  $B = 200\text{ T}$  the levels are completely filled up to the level  $n = 10$ ; for  $B = 500\text{ T}$  it happens the same only this time are filled up to the level  $n = 4$  and so on.

More interesting is the top and bottom of conduction and valence band of the zero field spectrum. In order to determine the cyclotron frequency for the three-band, through the derivation in Appendix C, we have obtained the Landau levels for the three-band model when the field is turned on Ta có thể thấy một số mức Landau có năng lượng là được tăng tuyến tính theo cường độ từ trường, nhưng lại không cách đều và chính xác như hình của Hofstadter butterfly. Thêm vào đó có nhiều trạng thái mà năng lượng tại đó thì giảm trong khi đó thì từ trường lại tăng. những trạng thái này sẽ được gọi là những trạng thái “kì cục” mà ta sẽ bàn luận ở đây.

Trong trường hợp một band, khối lượng hiệu dụng  $m^*$  và diện tích là đủ để mô tả được phổ Landau theo sự thay đổi tuyến tính của từ trường. Trong trường hợp 2 band và 3

band th

## 2.5 Chern number and Quantum Hall effect

### 2.5.1 Hall conductance

An electric field  $\mathbf{E}$  established in the solid results in an electric current  $\mathbf{I}$  linearly related to the field through Ohm's law

$$\mathbf{I} = \boldsymbol{\sigma} \mathbf{E}, \quad (2.52)$$

where  $\boldsymbol{\sigma}$  is the conductivity tensor. In two dimensional, there is a crucial relationship between the conductivity tensor  $\boldsymbol{\sigma}$  and the resistivity tensor  $\boldsymbol{\rho}$  is given by

$$\begin{bmatrix} \sigma_{xx} & \sigma_{xy} \\ \sigma_{yx} & \sigma_{yy} \end{bmatrix} \begin{bmatrix} \rho_{xx} & \rho_{xy} \\ \rho_{yx} & \rho_{yy} \end{bmatrix}^{-1} = \frac{1}{\rho_{xx}\rho_{yy} - \rho_{xy}\rho_{yx}} \begin{bmatrix} \rho_{yy} & -\rho_{xy} \\ -\rho_{yx} & \rho_{xx} \end{bmatrix}. \quad (2.53)$$

The contribution to the Hall conductance from a single subband is given by [10–13]

$$\sigma_{xy} = \frac{e^2}{h} \sum_n^{\text{occ.}} \frac{1}{2\pi} \oint_{\text{Bz}} dk_x dk_y \Omega_n^z(\mathbf{k}), \quad (2.54)$$

In general, the Berry curvature intergrated over a closed manifold is quantized in the units of  $e^2/h$  and equals to the net number of monopoles inside. This number is called the Chern number and is responsible for a number of quantization effects. Therefore the Hall conductivity is quantized for a two dimensional band insulator of noninteracting electrons.

### 2.5.2 Quantum Hall effect and Landau levels

With the cyclotron frequency in Section 2.4, the electron energy is quantized to the Landau levels

We calculate the quantum Hall conductivity by the Streda formula [14]

$$\sigma_{xy}(B, E_F) = e \frac{\partial \rho(E_F, B)}{\partial B}, \quad (2.55)$$

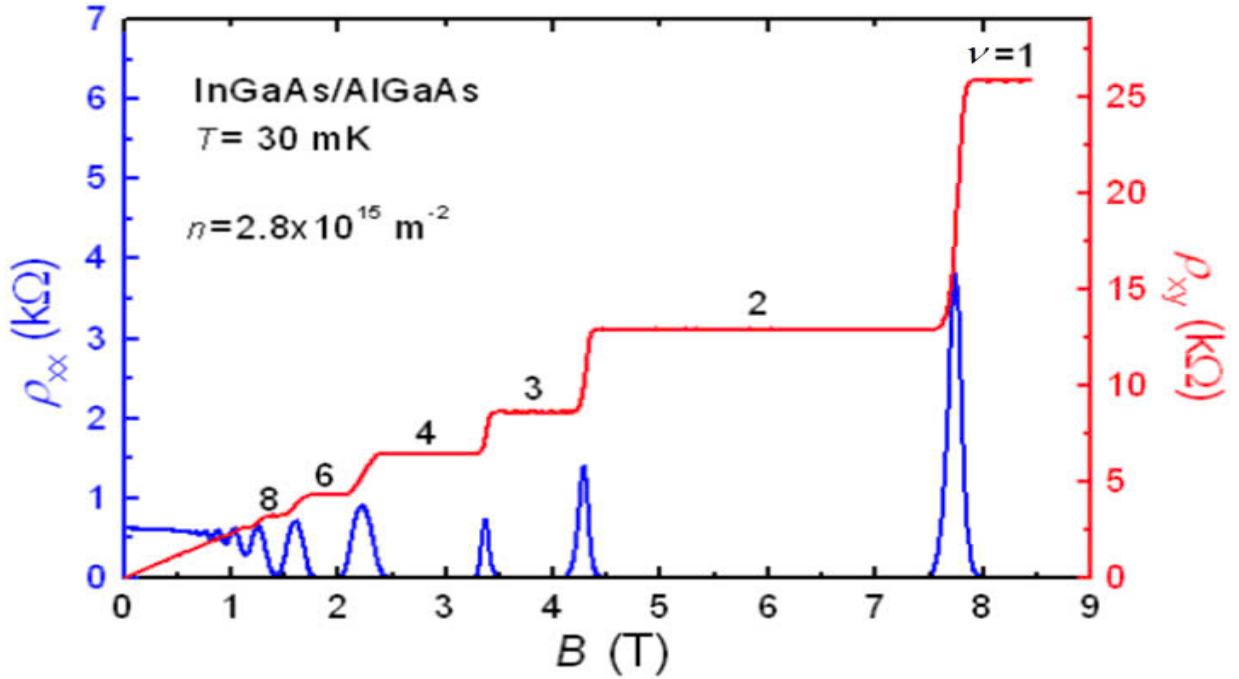
where  $\rho(E_F, B)$  is the cumulative energy density of state at Fermi-energy  $E_F$ . As show in Fig, the Hall conductivity is quantized at colored points. Since the intergral for the whole Brillouin zone respectively Berry curvature, we arrived at the Thouless-Kohmoto-

Nightingale-Nijs's formula (TKNN)

$$\sigma_{xy} = \frac{e^2}{h}\nu, \quad \nu = 1, 2, \dots \quad (2.56)$$

$\nu$  is guaranteed to be an integer given by the Chern number. Combining Eq(2.39) and Eq(2.40), we have

$$\frac{\partial \rho}{\partial B} = \frac{e}{h}\nu. \quad (2.57)$$



Hình 2.10: QHE

Assuming that  $B$  has slight variation

$$\rho = \text{const} + \frac{e}{h}B\nu. \quad (2.58)$$

Before this, we have defined  $\frac{p}{q} = \frac{eBa^2\sqrt{3}}{4h}$ , with  $S = \frac{\sqrt{3}a^2}{4}$  is the area of the unit cell. Multiply  $S$  with Eq(2.42), we have

$$\rho \times S = \text{const} + \frac{p}{q}\nu, \quad (2.59)$$

and the density of electron in a single band is given by  $\frac{1}{Sq}$ , thus when there are  $r$  band

below the Fermi energy level, the density of electron for  $r$ -th bands is

$$\rho = \frac{r}{Sq}. \quad (2.60)$$

The Eq(2.42), then, is written as,

$$r = \text{const} \times q + p \times \nu_r, \quad (2.61)$$

in this equation  $r, q, p, \nu_r$  are intergers, thus,  $\text{const} \times q$  must be an interger. On the one hand, since  $\text{const}$  is independent of  $q$ , and  $q$  can change when the magnetic field is varied without making a point of contact, then  $\text{const}$  itself must be an interger, namely  $s_r$ . Thus we have

$$r = q \times s_r + p \times \nu_r, \quad (2.62)$$

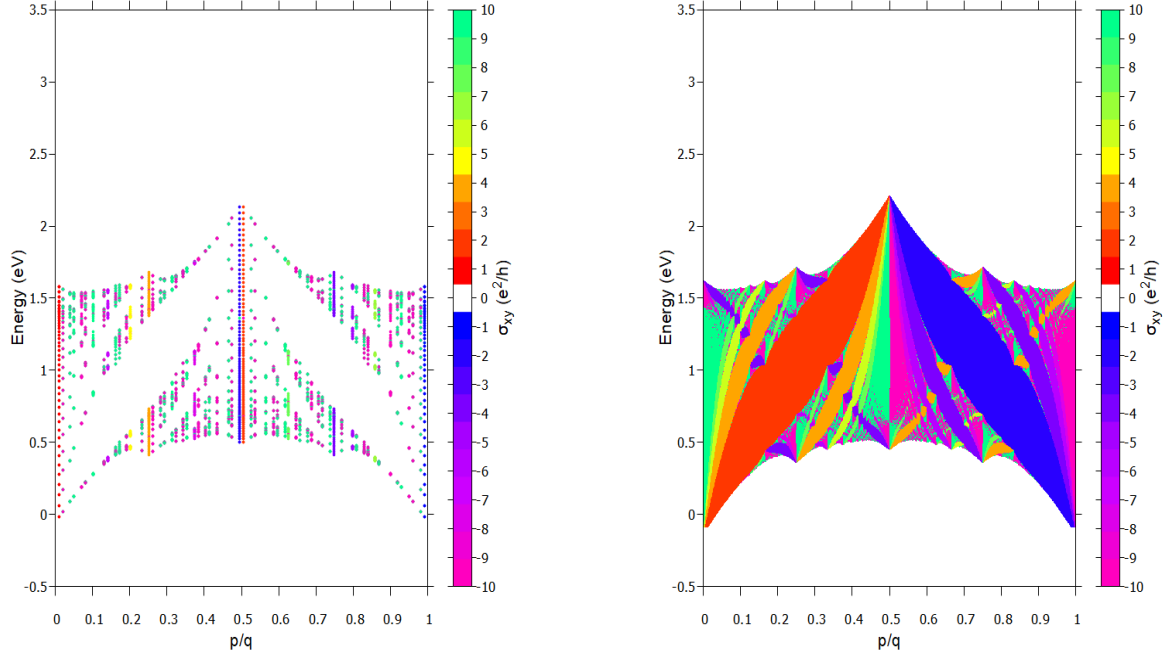
which is the Diophantine equation. In order to compute the Hall conductivity of the lattice model for a electron in a background magnetic field. We can only do this for rational fluxes  $\frac{\Phi}{\Phi_0} = \frac{p}{q}$ . In this case, we can use the TKNN formula, but with the Chern number, which used to be defined by intergrating over the Brillouin zone, now arising by intergrating over the magnetic Brillouin zone. Others derivation is in [15],[16].

The Hofstadter butterfly may be colored in a various ways. For instance, we may color the points of the butterfly by their Chern number, as illustrated in the Fig2.11(a). The disadvantage of this, is that there will be many points in the butterfly and so the fine details of the coloring may be obscured.

Fig 2.11(b) shows the Hofstadter butterfly, color-coded according to the Hall conductance. Moreover, the Chern number magnitude range will increase with  $q$  and so it is difficult to define a fixed scale. In this work, we uses a scale for Chern numbers with magnitude up to 10, as well as the color palette made famous by Avron *et al.* [17], which mean any Chern number out of range  $-10 \leq \nu \leq 10$  is equal to 10 or  $-10$ , respectively. Regions with zero Hall conductance and the corresponding spectrum are left blank. The two largest gaps in the center of the figure are associated with small intergers where the color coding is faithful. The colored picture emphasizes the gaps while the standard Hofstadter butterfly emphasis the spectrum. The colored figure is prettier and displays the regular aspects of the diagram: Gaps are better bahaved than spectra.

The transverse conductane in each energy gap, depicted in figure, is given by the sum of the Chern numbers of the occupied bands. At first discussed by Wannier in refernce [18], even a small change in the flux modifies radically the underlying band structure,





Hình 2.11: Từ trái sang phải là các Hofstadter butterfly, lần lượt là  $q = 99$  và  $q = 797$

thereby altering the intergrated density of states.

This results consistent with the Quantumm Hall effect and the Shubnikov-de Haas effects.

### 2.5.3 Solving the diophantine equation

We have defined that the magnetic flux through a unit cell is  $\frac{\Phi}{\Phi_0} = \frac{p}{q}$ . For  $p$  and  $q$  are mutually prime numbers, we defined the pairs  $(\nu_r, s_r) = (m, n)$  as the solutions

$$pm + qn = \gcd(p, q). \quad (2.63)$$

Fortunately,  $p$  and  $q$  are co-prime, Eq (2.47) is now

$$pm + qn = 1, \quad (2.64)$$

By deviding  $p$  by  $q$ , we get a quotient  $a$  and a remainder  $b$ . They satisfy

$$q = pa + b. \quad (2.65)$$

By using the Euclidean Algorithm, we can easily find  $(m, n)$ . For instance, the rational magnetic flux is  $\frac{p}{q} = \frac{30}{47}$ , then the diophantine equation now is  $30m + 47n = 1$ , and

$$\begin{aligned} 47 &= 30 \times 1 + 17, \\ 30 &= 17 \times 1 + 13, \\ 17 &= 13 \times 1 + 4, \\ 13 &= 4 \times 3 + 1. \end{aligned} \tag{2.66}$$

At this point we stop, because we arrived at the greatest common divisor, so the algorithm is over. The next step is solve for the remainders

$$\begin{aligned} 47 &= 30 \times 1 + 17 \Rightarrow 17 = 47 \times 1 + 30 \times (-1), \\ 30 &= 17 \times 1 + 13 \Rightarrow 13 = 30 \times 1 + 17 \times (-1), \\ 17 &= 13 \times 1 + 4 \Rightarrow 4 = 17 \times 1 + 13 \times (-1), \\ 13 &= 4 \times 3 + 1 \Rightarrow 1 = 13 \times 1 + 4 \times (-3). \end{aligned} \tag{2.67}$$

We are going to take this last remainder equation, and do backwards substitute until we get the very first remainder

$$\begin{aligned} 1 &= 13 \times 1 + 4 \times (-3) \\ &= 13 \times 1 + [17 \times 1 + 13 \times (-1)] \times (-3) \\ &= 13 \times 4 + 17 \times (-3) \\ &= [30 \times 1 + 17 \times (-1)] \times 4 + 17 \times (-3) \\ &= 30 \times 4 + 17 \times (-7) \\ &= 30 \times 4 + [47 \times 1 + 30 \times (-1)] \times (-7) \\ &= 30 \times (11) + 47 \times (-7), \end{aligned} \tag{2.68}$$

we find the solution for  $(m, n)$  is  $(11, -7)$ .

### 2.5.4 Wannier diagram

To further explore the intricate fractal nature of the Hofstadter spectrum, we shall now achieve a simplified replica of Fig. a powerful tool for visualizing the relationship between magnetic flux and electron filling in the system. Wannier's diagram provides a graphical representation of the allowed energy gaps in the Hofstadter spectrum as a function of the magnetic flux per unit cell and the electron filling factor. This diagram is particularly insightful because it captures the topological properties of the system through the distribution and behavior of these energy gaps.

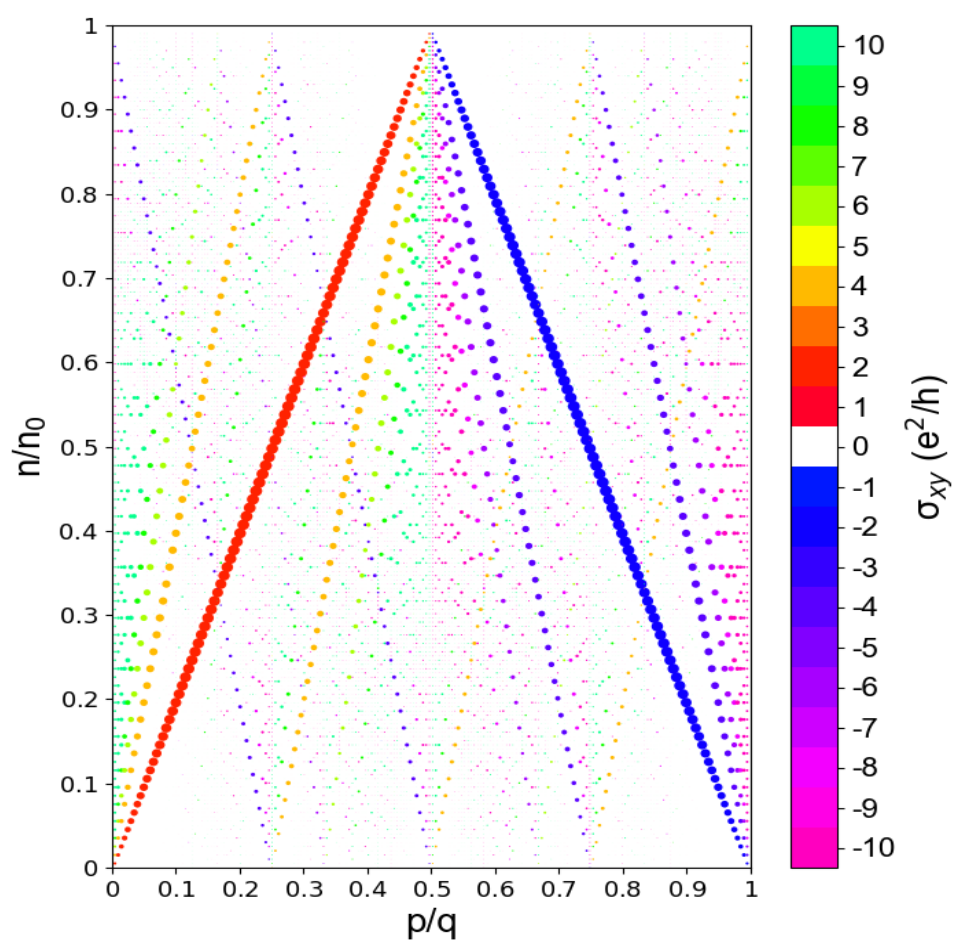
The fundamental of Wannier's diagram lies in the Diophantine gap equation

$$\frac{n}{n_0} = \nu \frac{\Phi}{\Phi_0} + s, \quad (2.69)$$

where  $\frac{n}{n_0}$  is the electron filling factor, representing the ratio of the number of electrons per unit cell,  $\nu$  is the Chern number associated with the quantized Hall conductance, and  $s$  is another integer that corresponds to the gap index, effectively indicating the electron filling within the spectrum.

The Diophantine equation is crucial in understanding the quantization of Hall conductance in the Hofstadter butterfly. The Chern number  $t$  determines the topological nature of the bands and their contribution to the Hall conductance, while the integer  $s$  identifies specific energy gaps in the spectrum. These gaps are directly linked to incompressible quantum Hall states, which are of significant interest in both theoretical and experimental condensed matter physics.

The calculated Wannier's diagram, the energy density of state as a function of filling factor  $\frac{n}{n_0}$  and magnetic flux  $\Phi$  as illustrated in Fig, reveal the presence of these energy gaps across the spectrum. Each colored line in the diagram corresponds to an energy gap where the system exhibits an incompressible quantum Hall state, characterized by a quantized Hall conductance. The diagram not only provides a clear visualization of the gap structure but also offers insights into the topological phases that arise in monolayer TMD systems under varying magnetic flux conditions.



Hình 2.12: Wannier diagram

## **CHƯƠNG 3**

### **RESULT AND DISCUSSION**

## **CHƯƠNG 4**

### **CONCLUSION AND FUTURE WORK**

In our research

## APPENDIX A

matrix

## APPENDIX B

### Harper's equation

Ta xét phương trình Harper cho trường hợp mạng tinh thể<sup>2</sup> là mạng vuông được cho bởi Hamiltonian từ ví dụ trong bài [2]

$$\begin{aligned} H(\mathbf{k}) &= 2t \left[ \cos(k_x a) + \cos(k_y a) \right] \\ &= t \left[ e^{ik_x a} + e^{-ik_x a} + e^{ik_y a} + e^{-ik_y a} \right] \end{aligned} \quad (\text{B.1})$$

Bằng cách áp dụng Peierls's substitution  $\mathbf{k} \rightarrow (\vec{p} - e\mathbf{A})/\hbar$ , ta có

$$\begin{aligned} H &= t \left[ e^{ik_x a} + e^{-ik_x a} + e^{i(p_y - eBx)a/\hbar} + e^{-i(p_y - eBx)a/\hbar} \right] \\ &= t \left[ e^{ik_x a} + e^{-ik_x a} + e^{ip_y a/\hbar} e^{i2\pi Bx/\Phi_0} + e^{-ip_y a/\hbar} e^{-i2\pi Bx/\Phi_0} \right] \end{aligned} \quad (\text{B.2})$$

Thay  $x = ma$  và  $y = na$  cho toạ độ của mạng tinh thể<sup>2</sup> vuông, ta thu được phương trình Harper

Let us consider the case of hexagonal lattice with  $|d_{z^2}\rangle$  band as a basis under an uniform magnetic field given by the Landau gauge  $\vec{A} = (0, Bx, 0)$ . Given



$$\begin{aligned}
h_0 &= 2t_0 (\cos 2\alpha + 2 \cos \alpha \cos \beta) + \epsilon_1 \\
&= 2t_0 \left[ \cos(k_x a) + 2 \cos\left(\frac{k_x a}{2}\right) \cos\left(\frac{\sqrt{3}k_y a}{2}\right) \right] + \epsilon_1 \\
&= 2t_0 \left\{ \cos(k_x a) + \cos\left[\left(k_x + \sqrt{3}k_y\right) \frac{a}{2}\right] + \cos\left[\left(k_x - \sqrt{3}k_y\right) \frac{a}{2}\right] \right\} + \epsilon_1 \\
&= 2t_0 \left\{ \cos\left(p_x \frac{a}{\hbar}\right) + \cos\left[\left(p_x + \sqrt{3}eBx + \sqrt{3}p_y\right) \frac{a}{2\hbar}\right] \right. \\
&\quad \left. + \cos\left[\left(p_x - \sqrt{3}eBx - \sqrt{3}p_y\right) \frac{a}{2\hbar}\right] \right\} + \epsilon_1 \\
&= t_0 \left[ e^{ip_x \frac{a}{\hbar}} + e^{-ip_x \frac{a}{\hbar}} + e^{i(p_x + \sqrt{3}eBx + \sqrt{3}p_y)a/2\hbar} + e^{-i(p_x + \sqrt{3}eBx + \sqrt{3}p_y)a/2\hbar} \right. \\
&\quad \left. + e^{i(p_x - \sqrt{3}eBx - \sqrt{3}p_y)a/2\hbar} + e^{-i(p_x - \sqrt{3}eBx - \sqrt{3}p_y)a/2\hbar} \right] + \epsilon_1.
\end{aligned} \tag{B.3}$$

We replaced  $\hbar k$  in the above function by the operators  $\vec{p} - e\vec{A}/c$  in order to create an operator out of  $h_0$ . When this substitution is made, the Hamiltonian element is seen to contain translation operators  $\exp[ap_x/\hbar], \exp[a\sqrt{3}p_y/(2\hbar)]$ . Depending on the gauge chosen, there are, in addition, certain phase factors dependent on the magnetic field strength, which multiply the translation operators. The Landau gauge was  $\vec{A} = (0, Bx, 0)$  was chosen, then only the translation along  $y$  are multiplied by phases. [3] Applying the BCH's formula and taking to account the commutation relation  $[x, p_x] = i\hbar$

$$\begin{aligned}
e^{\pm i(p_x + \sqrt{3}eBx)a/2\hbar} &= e^{\pm ip_x a/2\hbar} e^{\pm i\sqrt{3}eBxa/2\hbar} e^{-\frac{1}{2}[\pm ip_x, \pm i\sqrt{3}eBx]a^2/2\hbar^2} \\
&= e^{\pm ip_x a/2\hbar} e^{\pm i\sqrt{3}eBxa/2\hbar} e^{\mp i\sqrt{3}eBa^2/8\hbar}
\end{aligned} \tag{B.4}$$

Substituting  $x = \frac{ma}{2}$  into (B.2), this leads to

$$e^{\pm i(p_x + \sqrt{3}eBx)a/2\hbar} = e^{\pm ip_x a/2\hbar} e^{\pm i\sqrt{3}eB(m+1/2)a^2/4\hbar} \tag{B.5}$$

And

$$\begin{aligned}
e^{\pm i(p_x - \sqrt{3}eBx)a/2\hbar} &= e^{\pm ip_x a/2\hbar} e^{\mp i\sqrt{3}eBxa/2\hbar} e^{-\frac{1}{2}[\pm ip_x, \mp i\sqrt{3}eBx]a^2/2\hbar^2} \\
&= e^{\pm ip_x a/2\hbar} e^{\mp i\sqrt{3}eBxa/2\hbar} e^{\mp i\sqrt{3}eBa^2/8\hbar}
\end{aligned} \tag{B.6}$$

Substituting  $x = \frac{ma}{2}$  into (B.4), this leads to

$$e^{\pm i(p_x - \sqrt{3}eBx)a/2\hbar} = e^{\pm ip_x a/2\hbar} e^{\mp i\sqrt{3}eB(m-1/2)a^2/4\hbar} \tag{B.7}$$

The operators  $e^{\pm ip_x a/2\hbar}, e^{\pm ip_y \sqrt{3}a/2\hbar}$  can be regconized as translational operators, we can rewrite (B.3) as

$$\begin{aligned} & t_0\varphi_1(x+a, y) + t_0\varphi_1(x-a, y) + t_0\varphi_1(x + \frac{a}{2}, y + \frac{a\sqrt{3}}{2})e^{\frac{ie}{\hbar}B(m+1/2)\frac{a^2\sqrt{3}}{4}} \\ & + t_0\varphi_1(x + \frac{a}{2}, y - \frac{a\sqrt{3}}{2})e^{-\frac{ie}{\hbar}B(m+1/2)\frac{a^2\sqrt{3}}{4}} + t_0\varphi_1(x - \frac{a}{2}, y + \frac{a\sqrt{3}}{2})e^{\frac{ie}{\hbar}B(m+1/2)\frac{a^2\sqrt{3}}{4}} \quad (\text{B.8}) \\ & + t_0\varphi_1(x - \frac{a}{2}, y - \frac{a\sqrt{3}}{2})e^{-\frac{ie}{\hbar}B(m+1/2)\frac{a^2\sqrt{3}}{4}} + \epsilon_1\varphi_1(x, y) = E_1\varphi_0(x, y), \end{aligned}$$

for the sake of simplicity let us define  $\varphi_0 \equiv |d_{z^2}\rangle$ .

It is reasonable to assume planewave behavior in the  $y$  direction, since the coefficients in the above equation only involve  $x$ . Therefore, we can assume the partial solution for  $y$  to be in the form

$$\varphi(\frac{ma}{2}, \frac{na\sqrt{3}}{2}) = e^{ik_y n \frac{a\sqrt{3}}{2}} G(m), \quad (\text{B.9})$$

which reduces (B.6) to

$$\begin{aligned} & t_0\varphi_0(m+2) + t_0\varphi_0(m-2) + t_0\varphi_0(m+1)e^{2i\pi(m+1/2)p/q}e^{ik_y a\sqrt{3}/2} \\ & + t_0\varphi_0(m+1)e^{-2i\pi(m+1/2)p/q}e^{-ik_y a\sqrt{3}/2} + t_0\varphi_0(m-1)e^{2i\pi(m-1/2)p/q}e^{ik_y a\sqrt{3}/2} \quad (\text{B.10}) \\ & + t_0\varphi_0(m-1)e^{-2i\pi(m-1/2)p/q}e^{-ik_y a\sqrt{3}/2} + \epsilon_1\varphi_0(m) = E_1\varphi_0(m), \end{aligned}$$

this is equivalent to Eq. 2.16 we have mentioned in Section 2.2. Equation B.8 is sometimes called ‘‘Harper’s equation’’. [19] Since different  $m$  values give different equations, one reaches a unique set of equations when  $\Phi/\Phi_0$  is a rational number  $p/q$  and  $m$  goes through  $q$  different values, essentially resulting in the Hamiltonian matrix written for a magnetic unit cell enlarged in  $x$  direction  $q$  times.

Trong trường hợp của TMD của [1] đã đưa ra thì ta đã bỏ qua đi đóng góp của nguyên tử  $X$ , dẫn đến cấu trúc mạng tinh thể của TMD lục giác trở thành mạng tam giác bình thường và từ đó ta có thể mapping từ mạng tam giác thành trường hợp của mạng vuông. Ở mạng tam giác ta đã đưa ra được rằng các toán tử tịnh tiến phải tuân theo công thức Baker-Campbell-Hausdorff.

## APPENDIX C

### Cyclotron frequency for all band

Hamiltonian in the new basis read

$$\begin{aligned}\tilde{H}^{NN}(\mathbf{k}) &= WH^{NN}(\mathbf{k})W^\dagger \\ &= \begin{pmatrix} \frac{1}{2}(h_{11} + h_{22} + 2\text{Im}[h_{12}]) & \frac{1}{\sqrt{2}}(h_1^* + ih_2^*) & \frac{1}{2}(h_{11} - h_{22} + 2i\text{Re}[h_{12}]) \\ \frac{1}{\sqrt{2}}(h_1 - ih_2) & h_0 & \frac{1}{\sqrt{2}}(h_1 + ih_2) \\ \frac{1}{2}(h_{11} - h_{22} - 2i\text{Re}[h_{12}]) & \frac{1}{\sqrt{2}}(h_1^* - ih_2^*) & \frac{1}{2}(h_{11} + h_{22} - 2i\text{Im}[h_{12}]) \end{pmatrix}\end{aligned}\quad (\text{C.1})$$

Hamiltonian matrix element for the valence band now is

$$\begin{aligned}h_v &= \frac{1}{2}(h_{11} + h_{22} + 2\text{Im}[h_{12}]) \\ &= (t_{11} + t_{22})\cos 2\alpha + 2(t_{11} + t_{22})\cos \alpha \cos \beta \\ &\quad + 4t_{12}\sin \alpha(\cos \alpha - \cos \beta) + \epsilon_2 \\ &= (t_{11} + t_{22})\cos k_x a + 2(t_{11} + t_{22})\cos \frac{k_x a}{2} \cos \frac{\sqrt{3}k_y a}{2} \\ &\quad + 4t_{12}\sin \frac{k_x a}{2}(\cos \frac{k_x a}{2} - \cos \frac{\sqrt{3}k_y a}{2}) + \epsilon_2.\end{aligned}\quad (\text{C.2})$$

By using Taylor's expansion to second order of  $\mathbf{k}$  on (C.2) we have

$$\begin{aligned}h_v &\approx (t_{11} + t_{22})\left(1 - \frac{a^2 k_x^2}{2}\right) + 2(t_{11} + t_{22})\left(1 - \frac{a^2 k_x^2}{8}\right)\left(1 - \frac{3a^2 k_y^2}{8}\right) \\ &\quad - 4t_{12}\frac{ak_x}{2}\left(\frac{a^2 k_x^2}{8} - \frac{3a^2 k_y^2}{8}\right) + \epsilon_2 \\ &\approx 3(t_{11} + t_{22}) - \frac{3a^2(t_{11} + t_{22})}{4}(k_x^2 + k_y^2) - \frac{a^3 t_{12} k_x (k_x^2 - 3k_y^2)}{4} \\ &\quad + \frac{6a^4(t_{11} + t_{22})}{32}k_x^2 k_y^2 + \epsilon_2.\end{aligned}\quad (\text{C.3})$$

In this (C.3), we neglect coefficients of terms  $a^4$  by the small of large limit  $a$ , this leads to

$$h_v \approx 3(t_{11} + t_{22}) - \frac{3a^2(t_{11} + t_{22})}{4} (k_x^2 + k_y^2) - \frac{a^3 t_{12} k_x (k_x^2 - 3k_y^2)}{4} + \epsilon_2, \quad (\text{C.4})$$

and using substitution  $\hbar \mathbf{k} \rightarrow (\boldsymbol{\Pi} + e\mathbf{A})$

$$\begin{aligned} h_v \approx & 3(t_{11} + t_{22}) - \frac{3a^2(t_{11} + t_{22})}{4\hbar^2} \left[ \Pi_x^2 + (\Pi_y + eBx)^2 \right] \\ & - \frac{a^3 t_{12} \Pi_x [\Pi_x^2 - 3(\Pi_y + eBx)^2]}{4\hbar^3} + \epsilon_2, \end{aligned} \quad (\text{C.5})$$

Instead of doing as we have done in Section 2, there is an alternative way to determine the energy spectrum. The Hamiltonian can be simplified by a suitably chosen canonical transformation, or ladder (creation and annihilation) operators can be used instead of position and momentum operators, but the description of the motion in the  $xy$ -plane requires two commuting sets of operators now. Since  $x$  and  $\Pi_y$  appear together in the combination  $x + \frac{1}{eB}\Pi_x$ , the appropriate choice in this case is [20, 21]

$$\begin{aligned} a &= \sqrt{\frac{eB}{2\hbar}} \left( x + \frac{1}{eB}\Pi_y + \frac{i}{eB}\Pi_x \right), \\ a^\dagger &= \sqrt{\frac{eB}{2\hbar}} \left( x + \frac{1}{eB}\Pi_y - \frac{i}{eB}\Pi_x \right), \\ b &= \sqrt{\frac{eB}{2\hbar}} \left( y + \frac{1}{eB}\Pi_x + \frac{i}{eB}\Pi_y \right), \\ b^\dagger &= \sqrt{\frac{eB}{2\hbar}} \left( y + \frac{1}{eB}\Pi_x - \frac{i}{eB}\Pi_y \right). \end{aligned} \quad (\text{C.6})$$

The inverse transformation is then

$$\begin{aligned} x + \frac{1}{eB}\Pi_y &= \sqrt{\frac{\hbar}{2eB}} (a + a^\dagger), \\ \Pi_x &= i\sqrt{\frac{\hbar eB}{2}} (a^\dagger - a), \\ y + \frac{1}{eB}\Pi_x &= \sqrt{\frac{\hbar}{2eB}} (b + b^\dagger), \\ \Pi_y &= i\sqrt{\frac{\hbar eB}{2}} (b^\dagger - b). \end{aligned} \quad (\text{C.7})$$

It follows from the canonical commutation relations of the position and momentum

operators that the ladder operators satisfy bosonic commutation relations

$$[a, a^\dagger] = 1, \quad [b, b^\dagger] = 1, \quad (\text{C.8})$$

and

$$[a, a] = [a^\dagger, a^\dagger] = [b, b] = [b^\dagger, b^\dagger] = 0, \quad (\text{C.9})$$

moreover the operators  $a(a^\dagger)$  and  $b(b^\dagger)$  commute with each other, too. As in the usual one-dimensinal harmonic oscillator

$$a|n\rangle = \sqrt{n}|n-1\rangle, \quad a^\dagger|n\rangle = \sqrt{n+1}|n+1\rangle, \quad (\text{C.10})$$

where  $|n\rangle$  is an eigenstate of the usual number operators  $a^\dagger a|n\rangle = n|n\rangle$ , with  $n \geq 0$  an interger. In terms of them, the Hamiltonian (C.5) can be cast in form

$$\begin{aligned} h_v \approx & 3(t_{11} + t_{22}) - \frac{3a^2(t_{11} + t_{22})}{4\hbar^2} \frac{\hbar e B}{2} (-a^\dagger a^\dagger + a^\dagger a + a a^\dagger - a a) \\ & - \frac{3a^2(t_{11} + t_{22})}{4\hbar^2} \frac{\hbar e B}{2} (a a + a a^\dagger + a^\dagger a + a^\dagger a^\dagger) \\ & - \frac{a^3 t_{12}}{4\hbar^2} \frac{\hbar e B}{2} (-a^\dagger a^\dagger + a^\dagger a + a a^\dagger - a a) \Pi_x \\ & + \frac{a^3 t_{12}}{4\hbar^2} \frac{3\hbar e B}{2} (a^\dagger a^\dagger + a^\dagger a + a a^\dagger + a a) \Pi_x + \epsilon_2 \\ \approx & 3(t_{11} + t_{22}) - \frac{3a^2(t_{11} + t_{22})}{4\hbar^2} \frac{\hbar e B}{2} \end{aligned} \quad (\text{C.11})$$

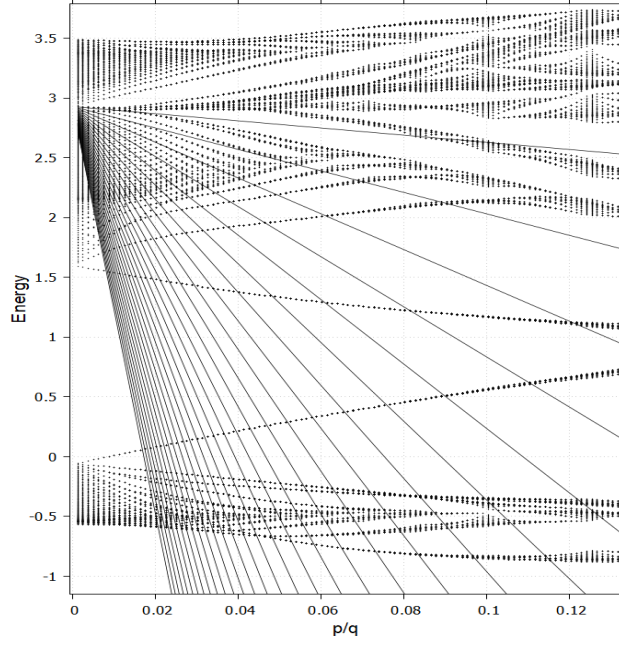
Tới đây thì không thể tính ra được vì còn số hạng bậc 3 theo  $kx$  và  $i$  có nghĩa là vẫn còn  $\Pi_x$ .

Tần số cyclotron khi sử dụng như section 2( đã loại bỏ số hạng có  $a^3$  và  $a^4$ )

$$w_c = \frac{eB}{m^*} = \frac{4\pi\sqrt{3}(t_{11} + t_{22})}{\hbar} \frac{p}{q}, \quad (\text{C.12})$$

and

$$E \approx (t_{11} + t_{22}) \left( 3 - 4\pi\sqrt{3} \frac{p}{q} (n + 1/2) \right) + \epsilon_2, \quad (\text{C.13})$$



Hình C.1: kết quả cho C.13

By using Taylor expansion, Hamiltonian Eq()

$$\begin{aligned}
h_0 &= t_0(6 - \frac{3}{2}a^2(k_x^2 + k_y^2)) + \epsilon_1 \\
h_1 &= 2it_1(\frac{3}{2}ak_x) - \frac{3}{2}t_2a^2k_xk_y \\
h_2 &= 2t_2(\frac{3}{8}a^2k_x^2 + \frac{3}{8}a^2k_y^2) + i3t_1ak_y \\
h_{11} &= (t_{11} + 3t_{22})(1 - \frac{1}{8}a^2k_x^2 - \frac{3}{8}a^2k_y^2) + 2t_{11}(1 - \frac{1}{2}a^2k_x^2) + \epsilon_2 \\
h_{22} &= (3t_{11} + t_{22})(1 - \frac{1}{8}a^2k_x^2 - \frac{3}{8}a^2k_y^2) + 2t_{22}(1 - \frac{1}{2}a^2k_x^2) + \epsilon_2 \\
h_{12} &= \sqrt{3}(t_{22} - t_{11})a^2k_xk_y
\end{aligned} \tag{C.14}$$

By using substitution  $\hbar\mathbf{k} = \mathbf{\Pi} + e\mathbf{A}$

$$\begin{aligned}
h_0 &= t_0(6 - \frac{3}{2\hbar^2}a^2(\Pi_x^2 + (\Pi_y + eBx)^2)) + \epsilon_1 \\
h_1 &= it_1\frac{3}{\hbar}a\Pi_x - \frac{3}{2\hbar^2}t_2a^2\Pi_x(\Pi_y + eBx) \\
h_2 &= 2t_2(\frac{3}{8\hbar^2}a^2\Pi_x^2 + \frac{3}{8\hbar^2}a^2(\Pi_y + eBx)^2) + i\frac{3}{\hbar}t_1a(\Pi_y + eBx) \\
h_{11} &= (t_{11} + 3t_{22})(1 - \frac{1}{8}a^2\Pi_x^2 - \frac{3}{8}a^2(\Pi_y + eBx)^2) + 2t_{11}(1 - \frac{1}{2}a^2\Pi_x^2) + \epsilon_2 \\
h_{22} &= (3t_{11} + t_{22})(1 - \frac{1}{8}a^2\Pi_x^2 - \frac{3}{8}a^2(\Pi_y + eBx)^2) + 2t_{22}(1 - \frac{1}{2}a^2\Pi_x^2) + \epsilon_2 \\
h_{12} &= \sqrt{3}(t_{22} - t_{11})a^2\Pi_x(\Pi_y + eBx)
\end{aligned} \tag{C.15}$$

$$\begin{aligned}
h_0 &= t_0(6 - \frac{3}{2\hbar^2}a^2(\Pi_x^2 + (\Pi_y + eBx)^2)) + \epsilon_1 \\
h_1 &= 2it_1\frac{3}{2\hbar}a\Pi_x - \frac{3}{2\hbar^2}t_2a^2\Pi_x(\Pi_y + eBx) \\
h_2 &= 2t_2(\frac{3}{8\hbar^2}a^2\Pi_x^2 + \frac{3}{8\hbar^2}a^2(\Pi_y + eBx)^2) + i\frac{3}{\hbar}t_1a(\Pi_y + eBx) \\
h_{11} &= (t_{11} + 3t_{22})(1 - \frac{1}{8}a^2\Pi_x^2 - \frac{3}{8}a^2(\Pi_y + eBx)^2) + 2t_{11}(1 - \frac{1}{2}a^2\Pi_x^2) + \epsilon_2 \\
h_{22} &= (3t_{11} + t_{22})(1 - \frac{1}{8}a^2\Pi_x^2 - \frac{3}{8}a^2(\Pi_y + eBx)^2) + 2t_{22}(1 - \frac{1}{2}a^2\Pi_x^2) + \epsilon_2 \\
h_{12} &= \sqrt{3}(t_{22} - t_{11})a^2\Pi_x(\Pi_y + eBx)
\end{aligned} \tag{C.16}$$

## REFERENCES

- [1] Gui-Bin Liu, Wen-Yu Shan, Yugui Yao, Wang Yao, and Di Xiao. Three-band tight-binding model for monolayers of group-vib transition metal dichalcogenides. *Phys. Rev. B*, 88:085433, Aug 2013.
- [2] Firat Yalçın. Tight binding investigation of graphene nanostructures under magnetic field. Master’s thesis, Middle East Technical University, 2019.
- [3] Douglas R. Hofstadter. Energy levels and wave functions of bloch electrons in rational and irrational magnetic fields. *Phys. Rev. B*, 14:2239–2249, Sep 1976.
- [4] James G. Analytis, Stephen J. Blundell, and Arzhang Ardavan. Landau levels, molecular orbitals, and the hofstadter butterfly in finite systems. *American Journal of Physics*, 72(5):613–618, 05 2004.
- [5] D. Shoenberg. *Magnetic Oscillations in Metals*. Cambridge Monographs on Physics. Cambridge University Press, 1984.
- [6] J. Singleton. *Band Theory and Electronic Properties of Solids*. Oxford Master Series in Condensed Matter Physics. OUP Oxford, 2001.
- [7] S. Blundell. *Magnetism in Condensed Matter*. Oxford Master Series in Condensed Matter Physics 4. OUP Oxford, 2001.
- [8] C. Kittel. *Quantum Theory of Solids*. Wiley, 1987.
- [9] Juan Li, Yi-Fei Wang, and Chang-De Gong. Tight-binding electrons on triangular and kagomé lattices under staggered modulated magnetic fields: quantum hall effects and hofstadter butterflies. *Journal of Physics: Condensed Matter*, 23(15):156002, apr 2011.
- [10] Mahito Kohmoto. Zero modes and the quantized hall conductance of the two-dimensional lattice in a magnetic field. *Physical Review B*, 39(16):11943, 1989.
- [11] Yasuhiro Hatsugai and Mahito Kohmoto. Energy spectrum and the quantum hall effect on the square lattice with next-nearest-neighbor hopping. *Physical review B*, 42(13):8282, 1990.



- [12] Mahito Kohmoto. Topological invariant and the quantization of the hall conductance. *Annals of Physics*, 160(2):343–354, 1985.
- [13] David J Thouless, Mahito Kohmoto, M Peter Nightingale, and Marcel den Nijs. Quantized hall conductance in a two-dimensional periodic potential. *Physical review letters*, 49(6):405, 1982.
- [14] P Streda. Theory of quantised hall conductivity in two dimensions. *Journal of Physics C: Solid State Physics*, 15(22):L717, 1982.
- [15] Francesco Di Colandrea, Alessio d’Errico, Maria Maffei, Hannah M Price, Maciej Lewenstein, Lorenzo Marrucci, Filippo Cardano, Alexandre Dauphin, and Pietro Massignan. Linking topological features of the hofstadter model to optical diffraction figures. *New Journal of Physics*, 24(1):013028, 2022.
- [16] Itzhack Dana, Yosi Avron, and J Zak. Quantised hall conductance in a perfect crystal. *Journal of Physics C: Solid State Physics*, 18(22):L679, 1985.
- [17] Joseph E Avron, Daniel Osadchy, and Ruedi Seiler. A topological look at the quantum hall effect. *Physics today*, 56(8):38–42, 2003.
- [18] GH Wannier. A result not dependent on rationality for bloch electrons in a magnetic field. *physica status solidi (b)*, 88(2):757–765, 1978.
- [19] Philip George Harper. The general motion of conduction electrons in a uniform magnetic field, with application to the diamagnetism of metals. *Proceedings of the Physical Society. Section A*, 68(10):879–892, 1955.
- [20] Jenő Sólyom. *Fundamentals of the Physics of Solids: Volume II: Electronic Properties*, volume 2. Springer Science & Business Media, 2008.
- [21] David J Griffiths and Darrell F Schroeter. *Introduction to quantum mechanics*. Cambridge university press, 2018.
- [22] Andor Kormányos, Viktor Zólyomi, Neil D. Drummond, Péter Rakyta, Guido Burkard, and Vladimir I. Fal’ko. Monolayer mos<sub>2</sub>: Trigonal warping, the  $\Gamma$  valley, and spin-orbit coupling effects. *Phys. Rev. B*, 88:045416, Jul 2013.
- [23] Fengyuan Xuan and Su Ying Quek. Valley zeeman effect and landau levels in two-dimensional transition metal dichalcogenides. *Phys. Rev. Res.*, 2:033256, Aug 2020.
- [24] Jun John Sakurai and Jim Napolitano. *Modern quantum mechanics*. Cambridge University Press, 2020.

- [25] Yakir Aharonov and David Bohm. Significance of electromagnetic potentials in the quantum theory. *Physical review*, 115(3):485–497, 1959.
- [26] Rudolph Peierls. Zur theorie des diamagnetismus von leitungselektronen. *Zeitschrift für Physik*, 80(11):763–791, 1933.
- [27] Gi-Yeong Oh. Energy spectrum of a triangular lattice in a uniform magnetic field: Effect of next-nearest-neighbor hopping. *Journal of the Korean Physical Society*, 37(5):534–539, 2000.